Tectonophysics 869 (2023) 230146

Contents lists available at ScienceDirect

Tectonophysics

journal homepage: www.elsevier.com/locate/tecto

Wedge plasticity and a minimalist dynamic rupture model for the 2011 M_W 9.1 Tohoku-Oki earthquake and tsunami

Shuo Ma *

Department of Earth and Environmental Sciences, San Diego State University, San Diego, CA, USA

ARTICLE INFO

Keywords:
Earthquake rupture dynamics
Tsunami generation
Inelastic wedge deformation
Energy sink
Slow rupture

ABSTRACT

One crucial yet unanswered question about the 2011 M_W 9.1 Tohoku-Oki earthquake and tsunami is what generated the largest tsunami (up to 40 m) along the Sanriku coast north of 39°N without large slip near the trench. A minimalist dynamic rupture model with wedge plasticity is presented to address this issue. The model incorporates the important variation of sediment thickness along the Japan Trench into the Japan Integrated Velocity Structure Model (JIVSM). By revising a heterogeneous stress drop model, the dynamic rupture model with a standard rate-and-state friction law can explain the GPS, tsunami, and differential bathymetry data (within data uncertainties) with minimum tuning. The rupture is driven by a large patch of stress drop up to ~10 MPa near the hypocenter with significantly smaller stress drop (< 3 MPa) in the upper ~10 km. The largest shallow slip reaches 75.67 m close to the trench north of hypocenter, which is caused by the large fault width, free surface, shallowly dipping fault geometry, and northwardly increasing sediment thickness, dominated by elastic off-fault response. North of large shallow slip zone, however, inelastic deformation of thick wedge sediments significantly controls the rupture propagation along trench, giving rise to slow rupture velocity (~850 m/s), diminishing shallow slip, and efficient seafloor uplift. The short-wavelength inelastic uplift produces impulsive tsunami consistent with the observations off the Sanriku coast in terms of timing, amplitude, and pulse width. Wedge plasticity and variation of sediment thickness along the Japan Trench thus provides a self-consistent interpretation to the along-strike variation of near-trench slip and anomalous tsunami generation in the northern Japan Trench in this earthquake.

1. Introduction

More than a decade of extensive research on the 2011 M_W 9.1 Tohoku-Oki earthquake and tsunami have revealed a clear picture of the earthquake rupture. >50 m of slip occurred near the trench up dip from hypocenter off Miyagi Prefecture, as resolved by many kinematic slip models using geodetic, seismic, and tsunami data (e.g., Sun et al., 2017; Lay, 2018; Uchida and Bürgmann, 2021; and references therein). More importantly, such large near-trench slip was confirmed by crucial data sets of differential bathymetry data before and after the earthquake (Fujiwara et al., 2011; Kodaira et al., 2012, 2020). There seems a consensus about this earthquake that large shallow slip at the trench caused large seafloor uplift that resulted in the devastating tsunami (e.g., Satake et al., 2013; Yamazaki et al., 2018; Lay, 2018; Uchida and Bürgmann, 2021). Large horizontal seafloor displacement of seafloor slopes driven by the large near-trench slip on a shallowly dipping plate interface also contributed significantly to the tsunami generation (e.g., Hooper et al., 2013).

However, one critical issue remains unsolved. The largest tsunami (up to 40 m) occurred along the Sanriku coast north of 39°N, causing immense devastations more than ~100 km north of the epicenter (Mori et al., 2011; Kodaira et al., 2021). The tsunami heights along the Sanriku coast were consistently several times larger than in the south, illustrated in Fig. 1a. Most slip models based on geodetic and seismic data failed to explain this important observation, shown by MacInnes et al. (2013), Tappin et al. (2014), and Yamazaki et al. (2018) among others, as these models resolved small or little slip north of ~38.5°N. In order to explain the large tsunami generation north of 39°N kinematic slip models based on tsunami data require near-trench slip up to 36 m (e.g., Satake et al., 2013; Yamazaki et al., 2018), which, however, violates the differential bathymetry observations in the northern Japan Trench (Fujiwara et al., 2017; Kodaira et al., 2020; Fujiwara, 2021; Zhang et al., 2023), indicating no large shallow slip near the trench nor large submarine landslides (Tappin et al., 2014). The turbidite data that shows correlation

* Corresponding author.
E-mail address: sma@sdsu.edu.

https://doi.org/10.1016/j.tecto.2023.230146
Received 12 June 2023; Received in revised form 5 November 2023; Accepted 16 November 2023
Available online 22 November 2023

with large shallow slip at trench off Miyagi Prefecture were also not observed north of ~38.7°N (e.g., Ikehara et al., 2018; Uchida and Bürgmann, 2021), consistent with the differential bathymetry data. The crucial differential bathymetry and turbidite data are summarized in Fig. 1b.

The differential bathymetry data in the northern Japan Trench, turbidite data, and the tsunami height distribution along the coast challenge the consensus that the devastating tsunami was generated by large shallow slip only. Without large shallow slip near the trench nor large submarine landslides, what produced the large tsunami north of 39°N? This is one crucial yet unanswered question (Kodaira et al., 2021). The key observations illustrated in Fig. 1 seem to suggest fundamentally different physics required to explain the 2011 Tohoku tsunami, which can have important implications for tsunami hazard assessments and reductions around the world. This crucial question is what the present study aims to address.

Nearly all the slip models for this earthquake are elastic dislocation models. However, several mechanisms can violate the assumption of elastic dislocation in the shallow subduction zone making elastic dislocation models less applicable (Wilson and Ma, 2021): (a) the overriding wedge may have low strength due to weak sediments in sediment-rich margins; (b) the outer wedge in accretionary margins subject to intense deformation geologically may be at or close to failure (e.g., Dahlen, 1990); (c) elevated pore pressure can be prevalent in the wedge due to low permeability of sediments (e.g., Saffer and Tobin, 2011); (d) the "thin-skinned" wedge geometry can result in large dynamic stress concentrations during earthquake rupture, especially near the toe; and (e) dynamic pore pressure increase due to updip rupture and increase of fault friction in the shallow velocity-strengthening region can weaken the wedge (Wang and Hu, 2006). These mechanisms can lead to inelastic deformation in the overriding wedge, producing deformation modes and rupture characteristics different from elastic dislocation models (e.g., Ma, 2012; Ma and Hirakawa, 2013; Ma and Nie, 2019; Wilson and Ma, 2021).

Seno (2000) and Tanioka and Seno (2001a, 2001b) first proposed the concept of inelastic deformation of sediments in causing efficient seafloor uplift with diminishing shallow slip on the fault. They modelled sediments as incompressible or fluidlike (Poisson's ratio = 0.49) materials. Ma (2012) and Ma and Hirakawa (2013) used a more realistic and rigorous constitutive framework and modelled inelastic deformation as undrained Mohr-Coulomb failure driven by dynamic stress field of rupture propagation. Importantly, they showed that inelastic wedge deformation is efficient in generating tsunami (due to frictional sliding on steep Coulomb microfractures) but meanwhile is a large energy sink

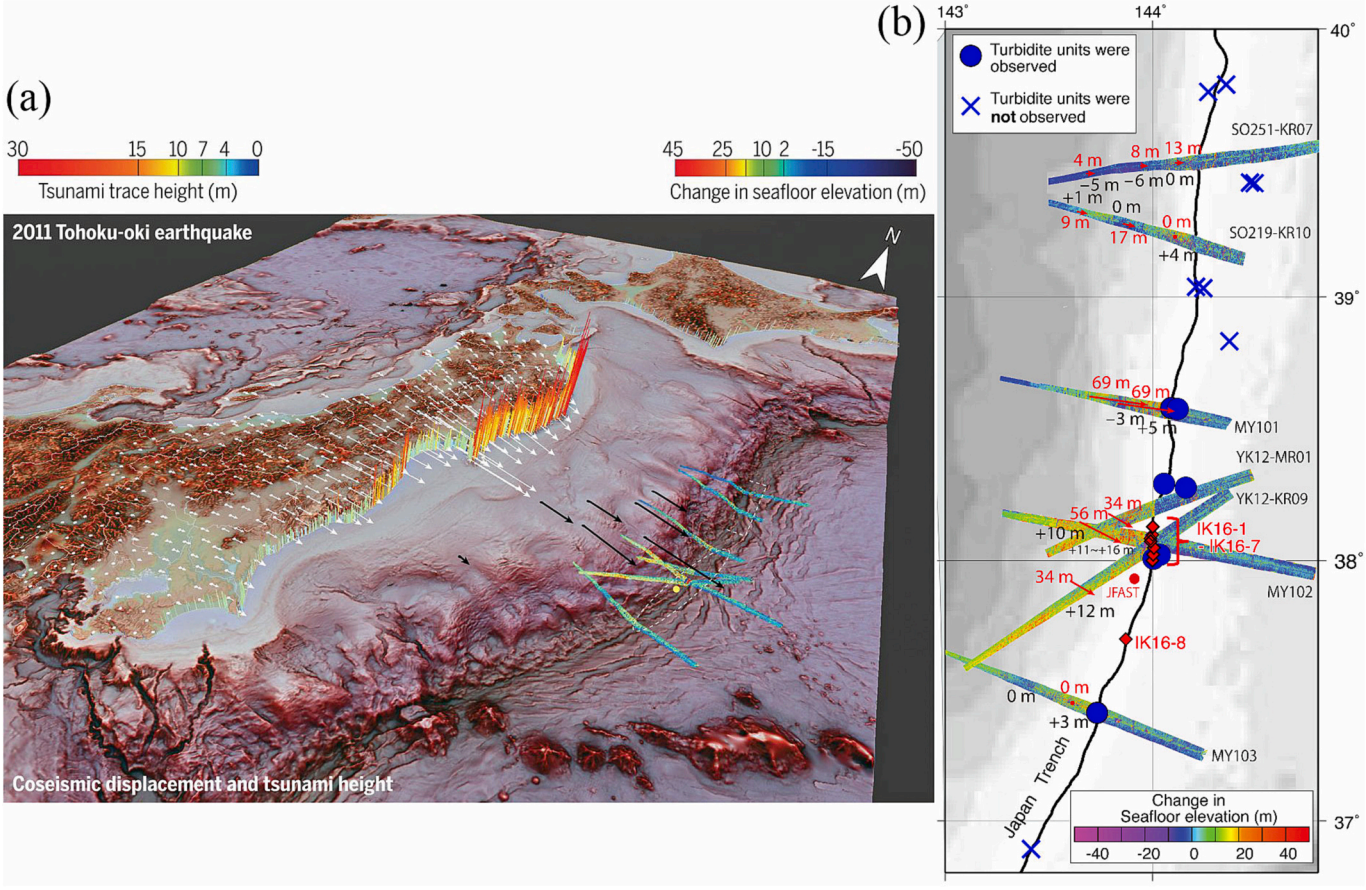

Fig. 1. (a) Coseismic displacements of the 2011 Tohoku-Oki earthquake recorded by GPS stations on land (white arrows) and seafloor (black arrows) and observed tsunami heights along the coast (from Kodaira et al., 2021). Note the much larger tsunami heights along the Sanriku coast. The scale of on-land displacement vectors is five times larger than that of offshore. The seven differential bathymetry profiles show the change in seafloor elevation. (b) Detailed coseismic horizontal (in red) and vertical (in black) seafloor displacements along the seven differential bathymetry profiles and the turbinate data observed along the Japan Trench (adapted from Uchida and Bürgmann, 2021). The resolutions of horizontal vertical displacement from the differential bathymetry data are ~20 m and a few meters, respectively. However, the data shows a distinctly different displacement pattern north of 39°N (with values within the uncertainties), ruling out the hypothesis of large near-trench slip in the northern Japan trench (Fujiwara et al., 2017; Fujiwara, 2021) and raising the question as to what generated the large tsunami along the Sanriku coast. The turbidite data (blue circles and crosses) show a similar pattern (Ikehara et al., 2018). North of ~38.7°N no turbidites were observed, suggesting no large shallow slip, consistent with the differential bathymetry data, while turbidites were observed in the large shallow slip region south of 38.7°N. (For interpretation of the references to colour in this figure legend, the reader is referred to the web version of this article.)

(due to plastic dissipation), leading to slow rupture propagation, high-frequency deficiency in seismic radiation, and low moment-scaled radiated energy, which have been anomalously observed for tsunami earthquakes (Kanamori, 1972) and the rupture characteristics in the shallow depths of large tsunamigenic earthquakes (e.g., Lay et al., 2012).

Ma and Nie (2019) extended the inelastic wedge deformation model to 3D by using a Drucker-Prager yield criterion (Drucker and Prager, 1952). The model was motivated by the variation of sediment thickness in the Japan Trench (e.g., Tsuru et al., 2002; Kodaira et al., 2017). They showed that in the northern Japan Trench where the sediment is thick inelastic deformation can produce efficient seafloor uplift with diminishing slip near the trench, while in the south where the sediment is thin the deformation is nearly elastic, causing large shallow slip and horizontal seafloor deformation. The model was for a Mw 8 earthquake, similar to the 1896 Sanriku earthquake (e.g., Tanioka and Seno, 2001b), but showed a mechanism capable of explaining the along-strike variation of near-trench slip in the 2011 Tohoku-Oki earthquake and anomalous tsunami generation in the northern Japan Trench consistent with the differential bathymetry observations. Using one inelastic wedge deformation model of Ma and Nie (2019), Du et al. (2021) showed that the short wavelength of inelastic uplift is capable of generating impulsive tsunami similar to what was observed off the Sanriku coast in 2011 (e.g., Maeda et al., 2011) and their model was able to explain the observed runup of the 1896 Sanriku tsunami without model tuning. Their results emphasized the importance of short-wavelength inelastic seafloor uplift in causing the extreme runup along the rugged Sanriku coast due to amplification of short-wavelength tsunami. Inelastic deformation has also been shown as an efficient tsunami generation mechanism for strike-slip earthquakes at fault complexities (e.g., restraining bends or stepovers), which may apply to the anomalous tsunami associated with the 2018 M_W 7.5 Palu earthquake (Ma, 2022).

Here I extend the model of Ma and Nie (2019) to model the dynamic rupture of the 2011 M_W 9.1 Tohoku-Oki earthquake. The model incorporates a 3D fault geometry and velocity structure based on the Japan Integrated Velocity Structure Model (JIVSM), which is widely used for modeling long-period strong ground motion in Japan (Koketsu et al., 2012). I use a heterogeneous stress drop model obtained from a kinematic slip distribution (Kubota et al., 2022) based on the same fault geometry from the JIVSM. The kinematic slip model inverted on- and off-shore GPS, and tsunami waveforms at offshore GPS buoys and 7 ocean bottom pressure (OBP) sensors located near the earthquake source region that became available recently. These new near-field tsunami waveforms place a tight constraint on the seafloor deformation and near-trench slip. The kinematic slip model of Kubota et al. (2022) is an elastic dislocation model in a homogenous half space. I incorporate the sediment thickness variation in the Japan Trench (Tsuru et al., 2002) in the JIVSM and consider possible inelastic deformation of wedge sediments during dynamic rupture process. The Strong Motion Generation Areas (SMGAs) identified by Kurahashi and Irikura (2013) are also added in the dynamic model as part of rupture process. I will show below that by revising the heterogenous stress drop model of Kubota et al. (2022) slightly and using a standard rate-and-state friction law, a minimalist dynamic rupture model can explain the GPS and tsunami data with minimum tuning. The seafloor deformation near the trench in the model is also in good agreement with the differential bathymetry observations. As suggested by Ma and Nie (2019), elastic off-fault response updip from the hypocenter and large fault width (~200 km) in the model lead to large near-trench slip (up to 75.67 m) extending ~200 km along trench off Miyagi Prefecture, enhanced by the free surface, shallow fault dip, and compliant wedge sediments (e.g., Ma and Beroza, 2008). However, north of ~38.5°N the rupture propagates onto a narrow fault (<50 km wide) along trench with thick overlying sediments, resulting in significant inelastic wedge deformation, which reduces shallow slip and increases seafloor uplift. The rupture velocity is as slow as ~850 m/s and stops naturally at ~39.8°N due to inelastic deformation. The slow rupture velocity and short-wavelength inelastic uplift will be shown to produce impulsive tsunami consistent with the observations off the Sanriku coast. This minimalist dynamic rupture model therefore provides a self-consistent interpretation to the along-strike variation of near-trench slip and the mystery of large tsunami generation off the Sanriku coast, consistent with the differential bathymetry and turbidite observations (Fig. 1).

Several dynamic rupture models for the 2011 Tohoku earthquake have been carried out to explore the physics of the earthquake. Using a realistic fault geometry and velocity structure 2D dynamic rupture model of Kozdon and Dunham (2013) highlighted that large shallow slip is possible even with a shallow velocity-strengthening region near the trench due to large dynamic stress of earthquake rupture on a ~ 200 km wide fault, enhanced by the free surface and shallowly dipping fault geometry. Duan (2012) and Tsuda et al. (2017) modelled 3D dynamic rupture on a planar fault and investigated the roles of subducted seamount in producing shallow slip and asperities in causing depth-dependent seismic radiation (e.g., Lay et al., 2012). These models were tested against little data. Galvez et al. (2019) modelled 3D dynamic rupture in a 1D velocity structure using a realistic fault geometry and simulated long-period ground motion (3–100 s) by using the SMGAs of Kurahashi and Irikura (2013). They carefully tuned the frictional parameters to match the timing of rupture in the SMGAs and produced long-period ground motion patterns at rock sites similar to the observations. All these models are elastic dislocation models, and none of them investigated the along-strike variation of near-trench slip and tsunami generation, which is the focus of this study.

2. Model

The same GPS and tsunami data sets in Kubota et al. (2022) are used in this work to constrain the dynamic rupture model (Fig. 2). Throughout the paper I use a coordinate system with x axis along the plate convergence direction (azimuth = 110°), y perpendicular to plate convergence direction (azimuth = 20°), and z vertical up, shown in Fig. 2c. The origin is located at the epicenter (38°06.2′ N, 142°51.6′E) taken from Satake et al. (2013). The plate convergence direction is obtained from DeMets et al. (2010), following Kubota et al. (2022). I consider a realistic fault geometry, bathymetry, and velocity structure based on the JIVSM. The original JIVSM fault geometry and bathymetry are defined on a regular grid with spacings 0.0125° along longitude and 0.0083° along latitude. I apply a moving average over 9 × 9 grid points and then down-sample both surfaces. The fault in the model is 200 km wide (along x) and 600 km long (along y), shown in Fig. 2c. The fault reaches the seafloor (at trench) at -200 km $\leq y \leq$ 300 km. The southern part of the fault ($y \leq$ -200 km) is buried because no shallow slip was found there, the top of the fault is located at 65 km (along x) landward from the trench.

As suggested by Ma and Nie (2019), the along-strike variation of sediment thickness in the Japan Trench (Tsuru et al., 2002) can play an important role in causing inelastic deformation leading to along-strike variation of near-trench slip and tsunamigenesis. Tsuru et al. (2002) provided the widths of sediment along seven seismic reflection profiles north of ~38°N. These seven profiles show that sediment thickness significantly increases from south to north, with sediment reaching up to 30 km wide from the trench and penetrating >10 km below the seafloor, forming large sedimentary prisms. Tsuru et al. (2002) also presented seven profiles south of ~38°N, but because the sediment is thin the widths of sediment were not provided. I choose 15 km and 20 km as the horizontal widths of the sediment on the seafloor and plate interface from trench (distances A and B in their notation) along these seven southern profiles by inspecting their reflection images. The widths of sediment along all fourteen profiles are then fit by a smooth backstop surface, shown by the yellow solid and dotted lines (traces of the backstop on the seafloor and plate interface) in Fig. 2. The increase of sediment thickness from south to north can be clearly seen. The JIVSM

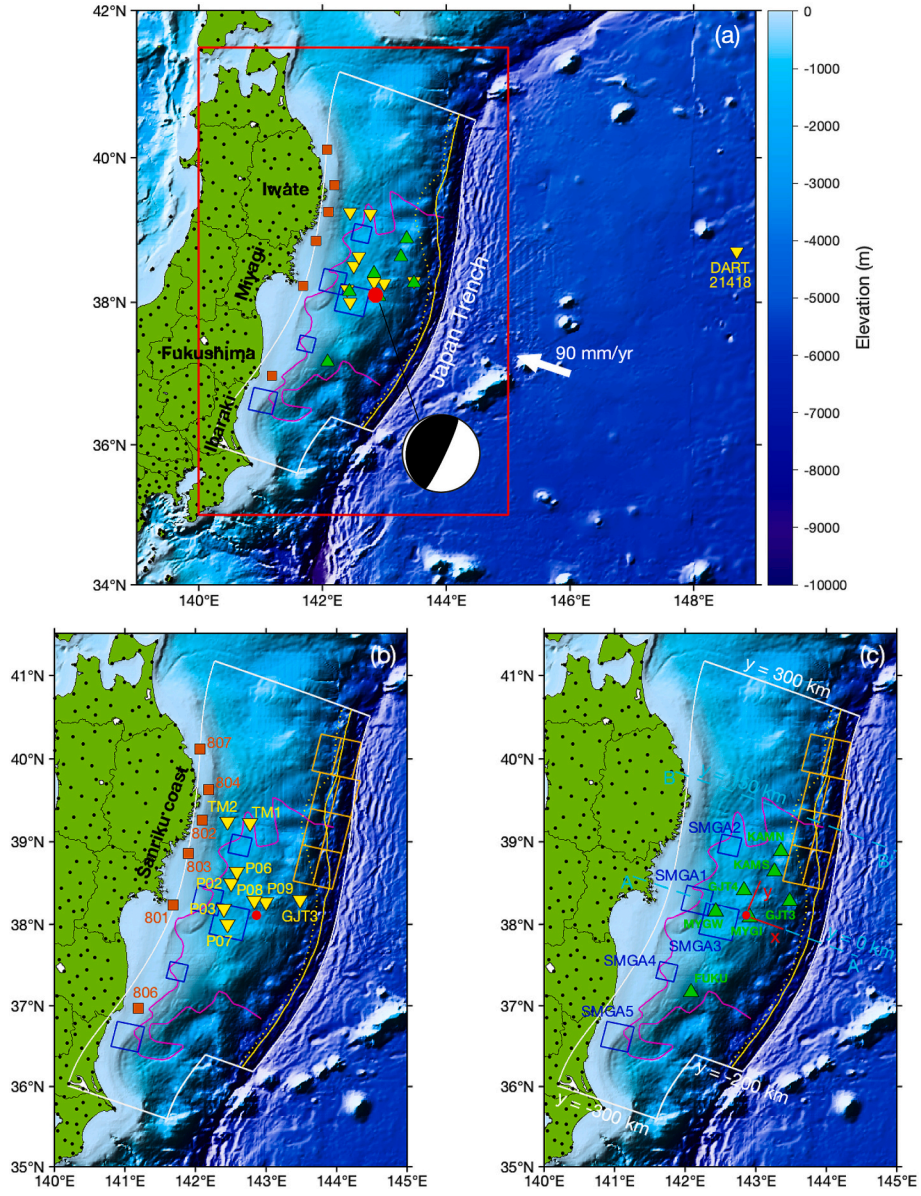

Fig. 2. Map of the region and the stations used in this work are shown: on-land GPS stations (black dots), GPS buoys (orange squares), OBP sensors (yellow inverted triangles), and off-shore GPS stations (green triangles). The red dot denotes the epicenter of the 2011 Tohoku-Oki earthquake and the beach ball shows the W-phase focal mechanism by the USGS. The magenta curve shows the coseismic rupture area inferred by Kato and Igarashi (2012). The blue squares are the SMGAs identified by Kurahashi & Irakura (2013). The fault surface used in this work is outlined by white. The yellow solid and dotted lines denote the traces of the backstop surface on the seafloor and plate interface by fitting the sediment-thickness data of Tsuru et al. (2002). Thicker sediments in the northern Japan Trench can be clearly seen. The large white arrow in (a) denotes the plate convergence direction based on DeMets et al. (2010). The red box in (a) marks the region shown in (b) and (c). The 8 subfaults of Satake et al. (2013) in the northern Japan Trench are shown in (b) and (c) to depict the rupture zone of the 1896 Sanriku earthquake. The coordinate system used in this work is shown in (c), where the origin is at the epicenter and x axis is along the plate convergence direction. The two cyan dashed lines ($y = 0$ and 150 km) denote the locations of two cross sections shown in Fig. 3. The four prefectures mentioned in the paper and the Sanriku coast are denoted in (a) and (b). GJT3 is the station name for both an OBP and seafloor GPS sensor, but the two sensors are not exactly collocated. Some identical features are shown in subsequent figures without further explanations. (For interpretation of the references to colour in this figure legend, the reader is referred to the web version of this article.)

does not include the sediment variation along the Japan Trench. I specify the material properties within the sedimentary wedge (seaward of backstop, i.e., outer wedge) to be $\rho = 2250$ kg/m^3, $V_P = 3000$ m/s, and $V_S = 1500$ m/s, where ρ, V_P, and V_S, are density, P- and S-wave velocities, respectively, corresponding to a shear modulus of 5.06 GPa, which is identical to the properties of layer 9 in the JIVSM. Material properties elsewhere use the JIVSM, which includes 23 spatially variable layers of uniform properties to mimic a three-dimensional structure. I set a minimum V_S to be 1000 m/s in the model to avoid too soft sediments near the surface to reduce the computational cost.

Fig. 3 shows two cross sections of the velocity structure used in the model. The subducting plate and the layered structure of the JIVSM are clearly seen. The fault sits on top of the oceanic crust and reaches the seafloor at the trench. In the JIVSM the top surface of the oceanic layer does not intersect with the seafloor at the trench. To make the fault reach the trench I move the top oceanic layer surface down slightly (0.2 km) and then add a 10° dipping plane from the trench along x to cut the fault surface. This 10° dipping plane can be seen in Fig. 3 but is more clearly seen in Movies S1 and 2. The choice of 10° is to avoid overly small timesteps in the simulations; the actual fault dip at the trench could be smaller. An extremely shallow fault dip (~4°) in the upper ~20 km is seen. A small sedimentary wedge at $y = 0$ and a much larger wedge at y

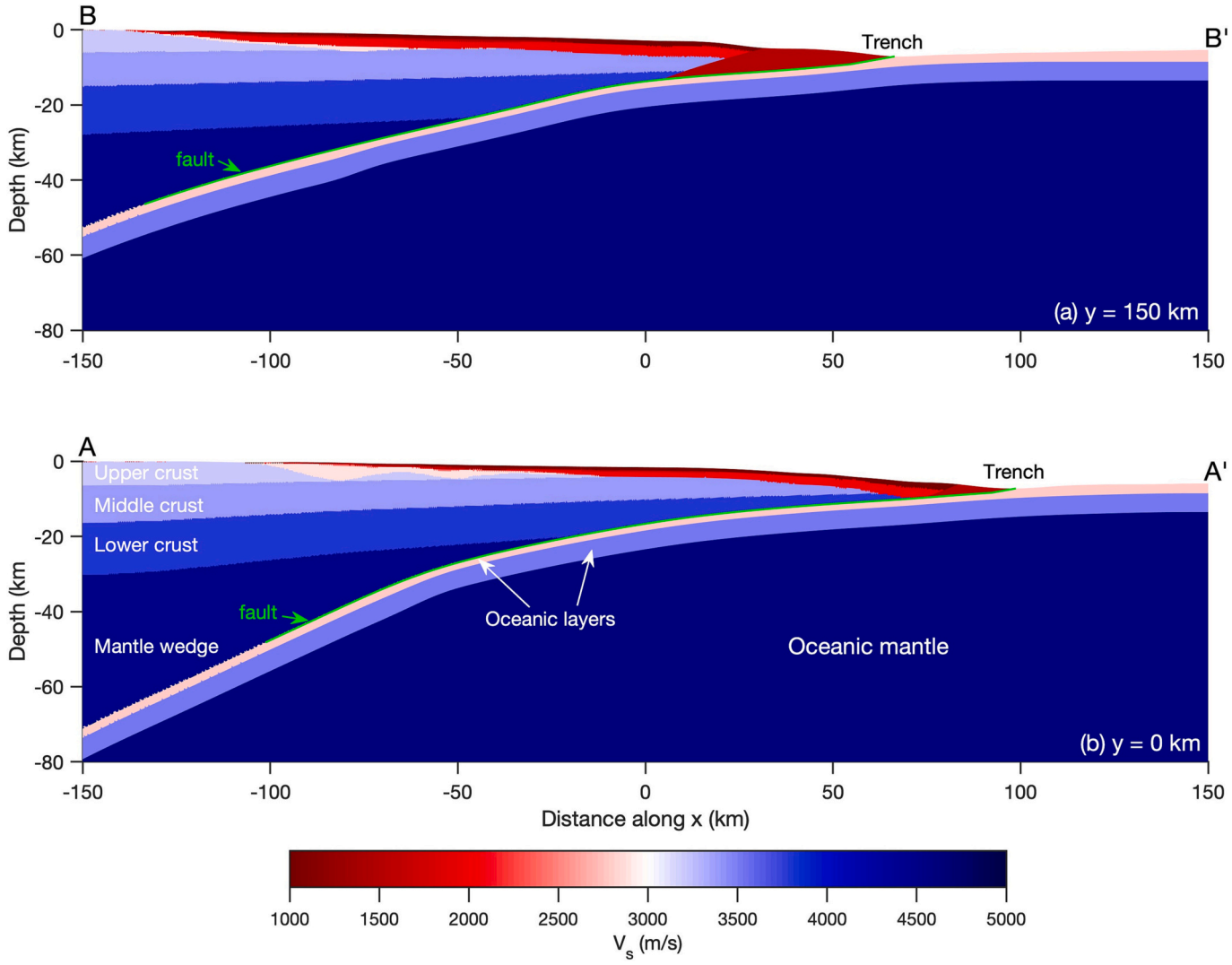

Fig. 3. Two cross sections of S-wave speed used in the velocity model are shown: (a) $y = 150$ km and (b) $y = 0$ km. No vertical exaggeration is used. The green curve in each panel shows the fault that reaches the seafloor at the trench. A small and large sedimentary wedge is seen at $y = 0$ km and $y = 150$ km, respectively. (For interpretation of the references to colour in this figure legend, the reader is referred to the web version of this article.)

= 150 km can also be clearly seen. In this work, the inelastic deformation in the outer wedge north of ~38.5°N will be shown to play a fundamental role in tsunami generation in the northern Japan Trench.

To model dynamic rupture on the fault, I use a regularized rate-and-state friction law with a slip law for the state evolution (e.g., Wilson and Ma, 2021). Specifically, shear stress on the fault τ relates to the regularized effective normal stress $\tilde{\sigma}$ by

$$\tau = f\tilde{\sigma}, \tag{1}$$

where the friction coefficient, f, on the fault is governed by

$$f(V,\psi) = a\sinh^{-1}\left[\frac{V}{2V_0}\exp\left(\frac{\psi}{a}\right)\right], \tag{2}$$

where V is slip velocity, V_0 is a reference slip velocity, a is the direct effect parameter, and ψ is the state variable that evolves according to the slip law:

$$\dot{\psi} = -\frac{V}{L}(\psi - \psi_{ss}), \text{and} \tag{3}$$

$$\psi_{ss} = a\ln\left[\frac{2V_0}{V}\sinh\left(\frac{f_{ss}}{a}\right)\right], \tag{4}$$

where over dot denotes time derivative, subscript ss denotes steady-state values, and L is the evolution distance. The steady-state state variable ψ_{ss} is a function of the steady-state friction f_{ss} that satisfies

$$f_{ss} = f_0 - (b-a)\ln\left(\frac{V}{V_0}\right). \tag{5}$$

This regularized friction law is well behaved at $V = 0$.The normal stress on the fault changes in the model due to the shallowly dipping fault geometry, heterogeneous velocity structure, and inelastic wedge deformation. I allow the regularized effective normal stress variable $\tilde{\sigma}$ to evolve towards the effective normal stress on the fault σ_N^* according to the same slip law:

$$\dot{\tilde{\sigma}} = -\frac{V}{L}(\tilde{\sigma} - \sigma_N^*). \tag{6}$$

By using $\tilde{\sigma}$ in Eq. (1) shear stress does not change instantaneously with normal stress change on the fault, consistent with some experimental data (e.g., Prakash, 1998).

For simplicity, the fault is assumed to slip at $V = V_0 = 1.0$ μm/s initially, impling that the initial friction coefficient is equal to reference friction f_0 and the fault is everywhere in a steady state initially. The

reference friction f_0 is assumed to be 0.25, which is about the median frictional values obtained from the JFAST drilling samples (e.g., Ikari et al., 2015; Hirono et al., 2016; Sawai et al., 2016). From Eq. (5), dynamic stress change after the breakdown process is completed can therefore be approximated by

$$\Delta\tau \approx (b-a)\ln\left(\frac{V}{V_0}\right)\sigma_N^{0,*}, \tag{7}$$

where $\sigma_N^{0,*}$ is the initial effective normal stress on the fault (the continuum mechanics convention is used). In the model, I choose some standard frictional values for a and b, and the shear stress change is directly proportional to $\sigma_N^{0,*}$ in the velocity-weakening region for simplicity. Heterogeneous a and b can also be used to infer $\sigma_N^{0,*}$, which, however, can affect rupture velocity and are not well constrained. I set $b = 0.014$ everywhere on the fault and the fault is assumed either velocity-weakening ($a = 0.01$) or velocity-strengthening ($a = 0.018$), thus $|a - b| = 0.004$ on the entire fault. If the dynamic stress change is known Eq. (7) can be used to infer $\sigma_N^{0,*}$. Note that this is only a crude way of estimating $\sigma_N^{0,*}$ because the normal stress changes on the fault in the model. To calculate dynamic stress change, the slip velocity V needs to be known. I assume $V = 1$ m/s. This choice of V does not affect the stress change significantly as stress change is a logarithmic function of V in Eq. (7).

I use a smoothed heterogeneous stress drop model of Kubota et al. (2022) shown in Fig. 4b, which was calculated from the slip distribution in a homogeneous half space (assuming shear rigidity of 40 GPa) by Kubota et al. (2022). Fig. 4a shows their smoothed slip distribution. The slip reaches a maximum value of 53 m at the trench updip from the hypocenter. Large slip extends ~200 km along both trench and fault dip in the central region off Miyagi Prefecture. The near-trench slip north of ~38.7°N is more modest (up to ~30 m) and the slip zone is rather narrow (<50 km wide). This slip distribution produced an excellent fit to the tsunami data recorded at the 7 OBP stations located near the major slip region, which places tight constraints on the slip distribution. This was the first study to use these data to constrain a slip model. The fit to the tsunami data at 6 near-shore GPS buoys is also very good. The model, however, underestimated the impulsive tsunami signal at TM1 and TM2 and GPS data on land. Kubota et al. (2022) also showed that the kinematic slip models of Iinuma et al. (2012), Satake et al. (2013), and Yamazaki et al. (2018) produced a poor fit to the tsunami data at the 7 OBP stations, questioning the validity of these models.

The stress drop in Fig. 4b is dominated by a large patch of stress drop up to ~10 MPa near the hypocenter. The stress drop updip from this large patch is significantly smaller (<~3 MPa); however, positive stress drop extends all the way to the trench. The stress drop in the northern near-trench region (north of ~39°N) reaches ~5 MPa in the shallow narrow slip zone. There is a band of large stress change region near the southwestern edge of the fault, which is not well resolved. Kubota et al. (2022) proposed that the large near-trench slip of 2011 Tohoku-Oki earthquake is mainly driven by the stress drop near the hypocenter and the free surface play a fundamental role in leading to large near-trench slip on a shallowly dipping fault (e.g., Fukuyama and Hok, 2015). The important effect of the free surface was also demonstrated in many other studies (e.g., Oglesby et al., 1998; Ma and Beroza, 2008; Kozdon and Dunham, 2013; Murphy et al., 2016; Yin and Denolle, 2021). Kubota et al. (2022) also showed that large stress drop at the shallow depths produces tsunami inconsistent with the OBP data, which may rule out the dynamic weakening mechanisms, such as thermal pressurization, at shallow depths (e.g., Noda and Lapusta, 2013).

Fig. S1 shows a distribution of initial effective normal stress on the fault calculated from the stress drop distribution in Fig. 4b and Eq. (7). In the calculation the stress drop is assumed along local dip only and shear stress along local strike is zero; during rupture the rake direction will change on the fault based on the absolute stress levels. I set $a - b = -0.004$ (velocity-weakening) for stress change less than -0.25 MPa and

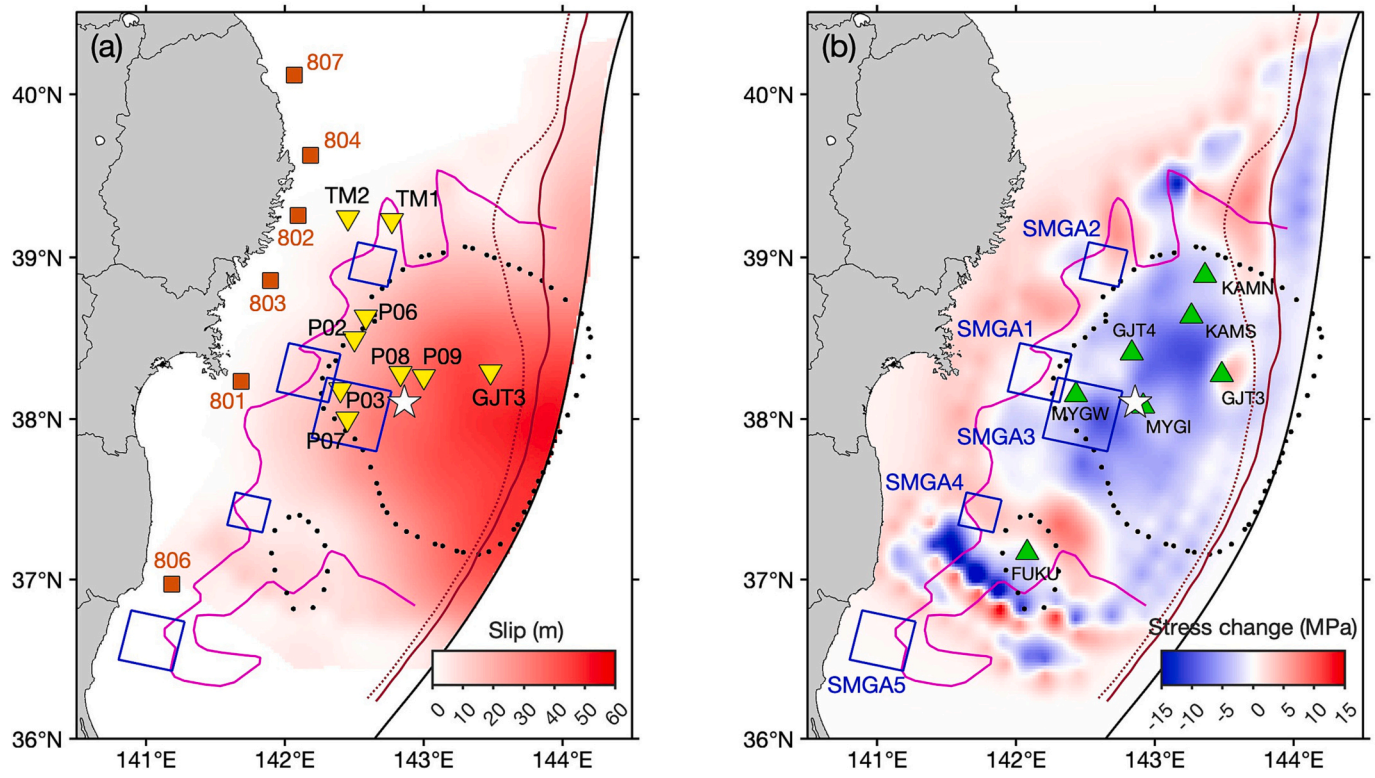

Fig. 4. The distributions of (a) slip and (b) static stress change for the 2011 Tohoku-Oki earthquake obtained by Kubota et al. (2022) are shown. The black dotted lines show the 15 m contours of the slip in Iinuma et al. (2012). The white star denotes the epicenter. (For interpretation of the references to colour in this figure legend, the reader is referred to the web version of this article.)

$a-b=0.004$ (velocity-strengthening) elsewhere. The stress change in the near-trench slip region north of ~38.5°N is reduced by $\frac{1}{3}$ because Kubota et al. (2022) did not consider the sediment in the region. The narrow band of large stress changes near the southwestern edge of the fault is removed because it is not well resolved, by setting $a-b=0.004$ (velocity-strengthening) at $y \leq$ -100 km. Three additional changes are made to the model shown in Figs. 4b and S1. An elliptical velocity-weakening region centered at ($x=-50$ km, $y=-175$ km) with the semimajor and semiminor axes of 80 km and 30 km, respectively, is added. The azimuth of the semimajor axis of the ellipse is 35°. The normal stress within the ellipse is set to be −60 MPa. This southwestern extension of velocity-weakening region is a robust feature of the coseismic rupture (e.g., Uchida and Bürgmann, 2021), coinciding with historic M7 earthquakes off Fukushima and Ibaraki Prefectures. It is also consistent with the coseismic rupture extent inferred from on-fault seismicity rate change (Kato and Igarashi, 2012). The second change to the model is to add the SMGAs of Kurahashi and Irikura (2013). Kurahashi and Irikura (2013) identified 5 SMGAs as the sources of strong motion and provided equivalent stress drop in each SMGA, which should be part of coseismic rupture process. Only the 4 SMGAs near the down-dip edge of the rupture zone are included in the model because SMGA3 is very close to the large stress drop patch near the hypocenter. The specified stress drops at SMGA1, SGMA2, SMGA4, and SMGA5 are 16.0, 20.0, 25.2, and 26.0 MPa, respectively, based on Kurahashi and Irikura (2013). Again, using Eq. (7) and $a-b=-0.004$ (velocity-weakening) the initial normal stress in each SMGA can be calculated. The southwestward extension of the rupture zone provides a pathway to break the SMGA5. A constant value $\sigma_N^{0,*}=-80$ MPa is assigned in the velocity-strengthening region of the fault to confine the rupture. The last minor change is that the normal stress on the velocity-weakening region of the fault within 5 km from the trench cannot be less than −5 MPa, to avoid too large stress drop near the trench. Finally, the distributions of $a-b$ and $\sigma_N^{0,*}$ are spatially smoothed by a moving average of 20 × 20 points on a 500 m uniform grid and then interpolated onto the fault, as shown in Fig. 5. After the smoothing there are narrow velocity-neutral regions ($a-b=0$) on the fault. Six cross sections of $a-b$ and $\sigma_N^{0,*}$ are shown in Fig. 6 to illustrate more details. The state variable evolution distance L is set to be 0.8 m on the fault except in the elliptical zone where L is 0.6 m. The same spatial smoothing is also applied and Fig. S2 shows the distribution of L on the fault used in the model. The smaller L in the ellipse is to allow rupture to break the SGMA5. This asperity is not easily breakable due to the large normal stress that leads to equivalently a large static friction. The rupture propagation is well resolved for most part of the fault except probably at the 4 SMGAs where the stress drop is large, as can be seen in Movies S1 and 2 shown in the next section.

With the frictional parameters and initial normal stress on the fault, rupture simulation with elastic off-fault response can be done. In order to incorporate inelastic deformation in the northern Japan Trench, absolute stress and pore pressure need to be specified in the wedge. In Ma and Nie (2019) the 2D critical stress solution of Dahlen (1984) was used, the maximum compressive stress was assumed perpendicular to wedge strike, and $\sigma_{yy}=0.5(\sigma_{xx}+\sigma_{zz})$. Here I derive an analytical solution for a

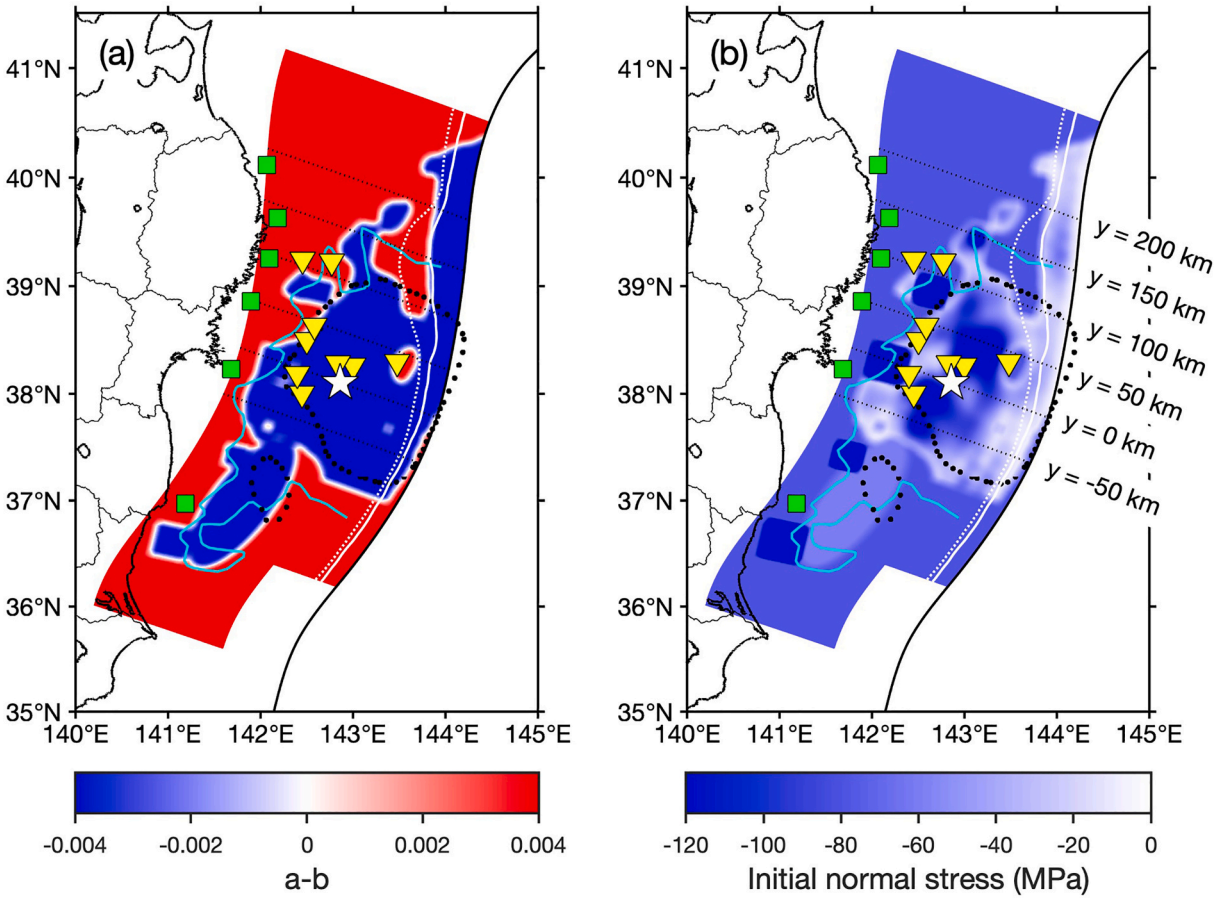

Fig. 5. The distributions of $a-b$ and initial effective normal stress used in the dynamic rupture models are shown. The velocity-weakening region ($a-b<0$) extends all the way to the trench over a large shallow portion of the fault. There is a small velocity-strengthening region near station GJT3. A southwestward extension of the velocity-weakening region and 4 SMGAs can be clearly seen. The normal stress is linearly related to dynamic stress change according to Eq. (7). The dotted lines show the cross sections plotted in Fig. 6. Similar cross sections are shown in subsequent figures. (For interpretation of the references to colour in this figure legend, the reader is referred to the web version of this article.)

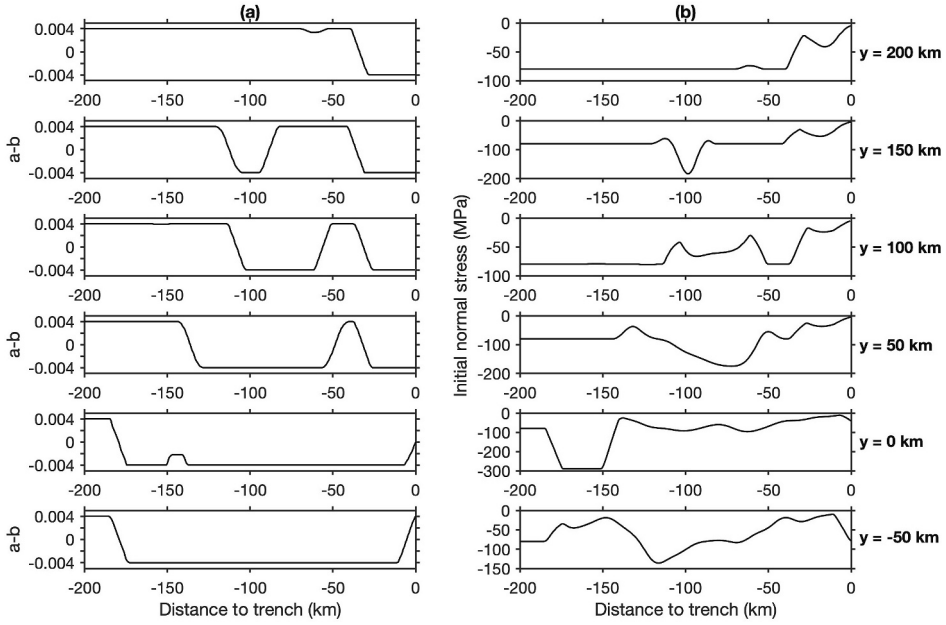

Fig. 6. Distributions of $a-b$ and initial effective normal stress at 6 cross sections are shown.

3D cohesionless critical wedge subject to the Drucker-Prager yield criterion in Appendix A, which is a general solution for an arbitrary maximum compressive direction and relaxes the assumptions made in Ma and Nie (2019). The Drucker-Prager yield criterion is given by

$$\sqrt{0.5 s_{ij} s_{ij}} = c\cos\phi - \frac{\sigma^*_{kk}}{3}\sin\phi, \tag{8}$$

where s_{ij} is deviatoric stress, c is cohesion, ϕ is internal frictional angle, and asterisk denotes effective stress. The 3D critical wedge solution gives the complete stress field, pore pressure, and internal friction in a cohesionless wedge when the direction of maximum compressive stress and basal friction are specified. The 3D solution can also provide the stress on the fault if the pore pressure on the fault is known. In this work, the stress on the fault is obtained from the heterogeneous stress drop and the rate-and-state friction described above, which can be thought of as a proxy of heterogeneous pore pressure on the fault, heterogeneous material properties in the wedge, and other fault zone complexities not captured by the simple critical wedge model (see Appendix A).

In order to move the wedge away from failure initially the cohesion is added in the model by using a closeness-to-failure (CF) parameter

$$CF = \sqrt{0.5 s^0_{ij} s^0_{ij}} \Big/ \left(c\cos\phi - \frac{\sigma^{0,*}_{kk}}{3}\sin\phi \right), \tag{9}$$

where superscript 0 denotes initial stresses.

I allow inelastic deformation to occur within 65 km landward from the trench in the overriding wedge for $y > 0$. No inelastic deformation is allowed for $y < 0$ because sediments are thin, so $CF = 0$ (i.e., infinite cohesion). Motivated by the variation of sediment thickness the CF in the outer wedge is specified to vary smoothly as a cosine function from CF_s to CF_n, i.e.,

$$CF(y) = \begin{cases} CF_n, y > y_w \\ \dfrac{CF_n + CF_s}{2} + \dfrac{CF_n - CF_s}{2}\cos\left[\dfrac{\pi}{y_w}(y - y_w)\right], 0 \le y \le y_w \\ 0, y < 0 \end{cases}, \tag{10}$$

where CF_s is 0.1 and CF_n is 0.9, and y_w is 150 km in the model. The CF in the inner wedge (between within 65 km landward from trench and the backstop) is set to be 0.1 for $y > 0$. The specified CF here varies from 0.1 to 0.9 from $y = 0$ to $y = 150$ km in the outer wedge, so large CF values are only around the northern Japan Trench, where significant inelastic wedge deformation can occur. Elsewhere small inelastic wedge deformation can be expected due to low CF values. Therefore, the inelastic and elastic models to be shown below differ mostly only in the northern Japan Trench; elsewhere the wedge deformation is nearly elastic. Other CF values have also been explored (results not shown). For larger CF_s (say 0.3) the slip at the trench updip from the hypocenter is becoming diminished by inelastic deformation, inconsistent with the differential bathymetry data. When CF_n increases to 0.95 the rupture fails to propagate into the northern Japan Trench due to severe inelastic deformation. When CF_n is 0.85 the results are similar to the elastic case. So, there is a narrow range of CF_n in the model to produce the results consistent with observations. The CF used here is only a crude way of characterizing wedge strength. In the future, the model can perhaps be improved by incorporating realistic strength parameters to replace the use of CF.

The important effect of undrained pore pressure change is included in the model as it can significantly affect yielding (Viesca et al., 2008; Ma and Nie, 2019), i.e.,

$$\dot{p} = -B\frac{\dot{\sigma}_{kk}}{3}, \tag{11}$$

where p is pore fluid pressure, B is the Skempton's coefficient, and no inelastic volumetric deformation is assumed (e.g., Andrews, 2005). The undrained inelastic dilatancy tends to strengthen the material that reduces inelastic deformation (e.g., Viesca et al., 2008), while undrained inelastic compaction tends to weaken the material that increases inelastic deformation (e.g., Hirakawa and Ma, 2016). It is not well understood how the inelastic volumetric deformation behaves for high-porosity sediments likely in the outer wedge during large strain rates. In this simple model, inelastic deformation is assumed to occur only in shear. During plastic flow each deviatoric stress is adjusted by the same ratio to move the stress back to the yield surface and there is no plastic hardening or softening (Andrews, 2005; Ma and Andrews, 2010). The Biot's and Skempton's coefficients are assumed to be 0.5 and 0.6, respectively, which are modest values for sediments (e.g., Wang, 2000). The Biot's coefficient is only used in the model to calculate undrained bulk moduli.

The rupture is nucleated at the hypocenter by applying a 2D Gaussian perturbation in shear stress over 1 s on the fault (the standard

deviation and the peak amplitude of the Gaussian function are 6000 m and 15% of the background shear stress, respectively).

I use the same finite-element code used in Ma and Nie (2019). The finite-element mesh uses 4-node tetrahedral elements only. The fault and inner and outer wedges are meshed by element size ~500 m. The mesh is smoothly coarsened away from the fault towards a remote boundary (~5000 km away) to prevent spurious reflections from the boundary and ensure an accurate static field. The time step of the

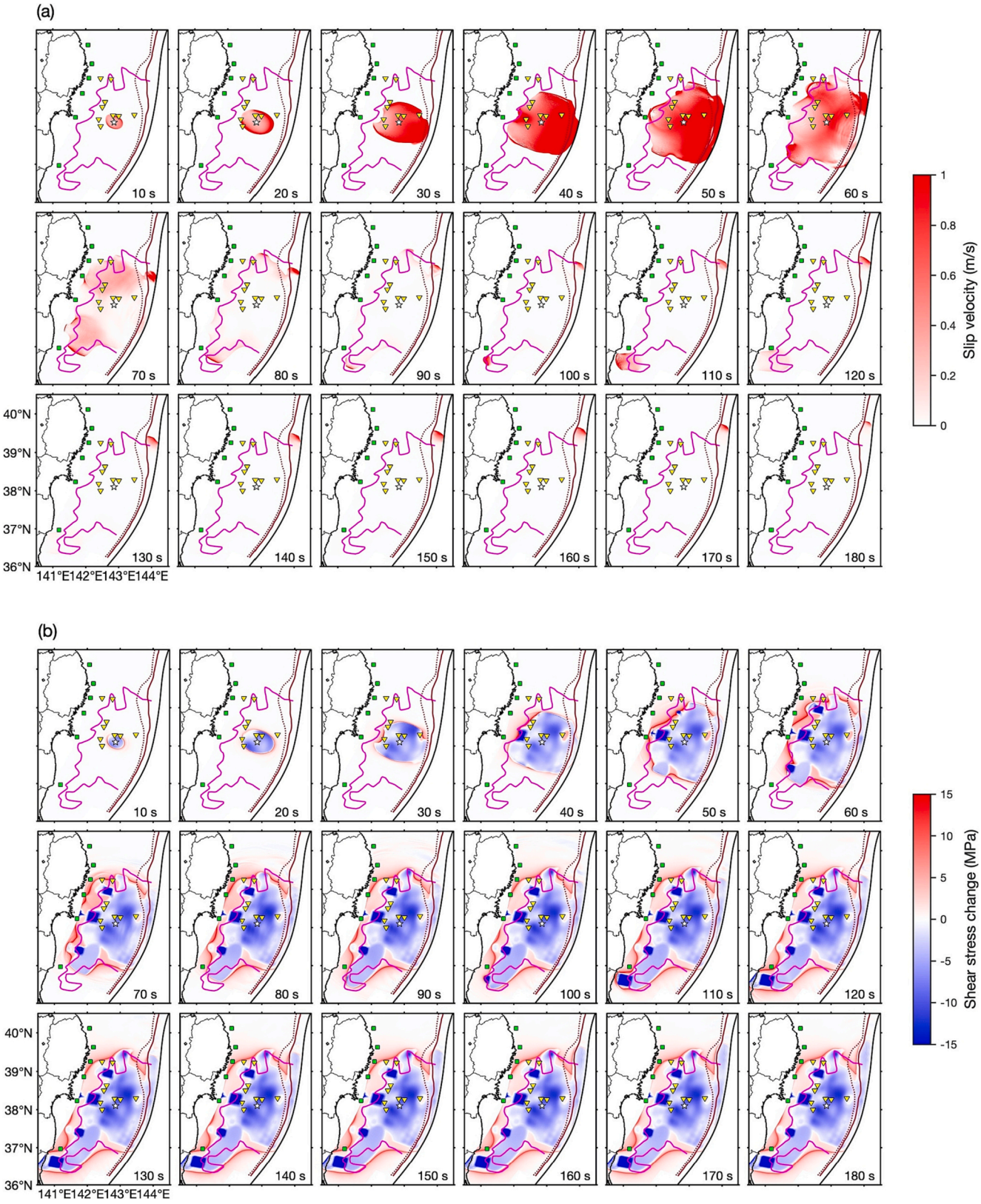

Fig. 7. The snapshots of (a) slip velocity, (b) shear stress change, and (c) slip every 10 s are illustrated on the fault for the inelastic model. The colour is saturated. (For interpretation of the references to colour in this figure legend, the reader is referred to the web version of this article.)

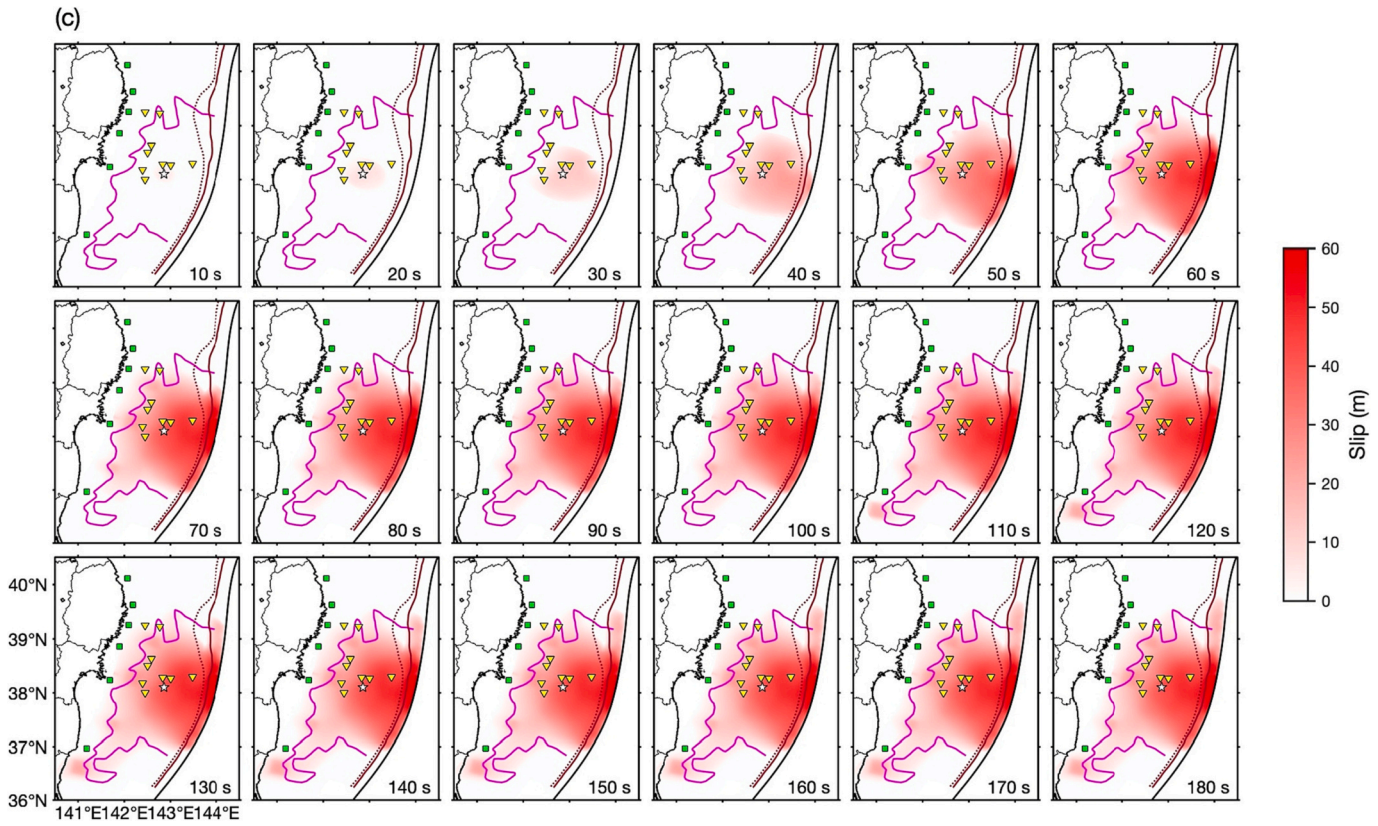

Fig. 7. (*continued*).

simulations is 0.01 s. All the simulations are run for 480 s to allow seismic waves to propagate out of the domain of interest.

3. Results

I start by showing the snapshots of slip velocity, shear stress change, and slip for the inelastic case ($CF_n = 0.9$) in Fig. 7. More detailed rupture process is illustrated in Movie S1. After the nucleation, the rupture propagates in all directions with a faster rupture velocity in mode II (along dip) direction. The rupture is driven by the large stress drop patch near the hypocenter (up to ~10 MPa). Because the large stress drop patch is mainly along strike, the peak slip velocity reaches over 10 m/s in the along-strike direction, but the rupture velocity is slower. The overall rupture velocity is subshear (~3 km/s). Shortly after 20 s, the updip rupture front accelerates although the stress drop at shallow depths is small. The acceleration of the rupture front is caused mainly by the free surface and the low normal stress (i.e., low static friction) at shallow depths (Fig. 5b). It should be noted that nearly entire updip region off Miyagi Prefecture from the hypocenter (except for a small region near station GJT3) as well as in the northern Japan Trench is velocity-weakening in the model (Fig. 5a), which can be due to the presence of horst-and-graben structures on the plate interface enhancing fault coupling (e.g., Polet and Kanamori, 2000). Due to small *CF* the wedge response in the central region is mostly elastic. The rupture breaks the trench at about 38 s with a peak slip rate 18.21 m/s, causing large horizontal displacement over 50 m and vertical displacement over 10 m near the trench (mostly on the 10° dipping fault segment). The rupture then expands along the trench northward and southward. Large slip rate > 50 m/s can be seen near the trench locally. The southward rupture along trench stops at ~70 s when it enters the southern velocity-strengthening region near $y = -100$ km. The northward rupture produces even larger slip, and horizontal and vertical displacements around $y = 50$ km, which is due to the northwardly increasing sediment thickness. The compliant hanging wall and free surface significantly enhance the dynamic stress drop and slip when the off-fault response is elastic (Ma and Beroza, 2008). However, when the rupture propagates further north into the narrow slip zone with thicker sediments (larger *CF*) a surprising slow rupture propagates along the trench with diminishing shallow slip and long rupture duration, and naturally dies out at ~39.8°N at ~200 s. The large difference in near-trench slip between central large-slip region and northern Japan Trench is evident.

The down-dip rupture is mainly governed by the breaking of the 4 SMGAs and the elliptical velocity-weakening zone. At ~20 s, the rupture reaches SMGA1. However, due to the large normal stress at the SMGA the static friction caused by the direct effect in the rate-and-state friction is also large. The rupture stalls for ~15 s and wraps around the asperity, and then finally breaks it with large stress drop and local supershear rupture velocity, which is similar to the result reported by Dunham et al. (2003) but using a rate-and-state friction. The down-dip rupture propagates laterally to the north and south. The northeastward rupture breaks the SMGA2 similarly and eventually stops at ~39.5°N. The southwestward rupture enters the elliptical velocity-weakening zone at ~36 s and breaks SMGA4 and SMGA5 again with large stress drop and local supershear rupture velocity and stops at 140 s while the slow northward rupture continues along the northern Japan Trench.

A space-time plot of slip velocity and shear stress change through the hypocenter ($y = 0$) illustrates these features in the updip and downdip directions more clearly (Fig. 8). The acceleration of rupture front at shallow depths and strong breakout phase at the trench can be seen. The reflections propagating downdip from the trench can be seen, but quickly die out in the model. The stalling of rupture at SMGA1 and the ensuing supershear rupture velocity and large stress drop are also clearly seen.

It should be noted that the rupture times (or rupture velocities) on the central and southwestern parts of the fault and the SMGAs are probably not well constrained by the GPS and tsunami data. No effort

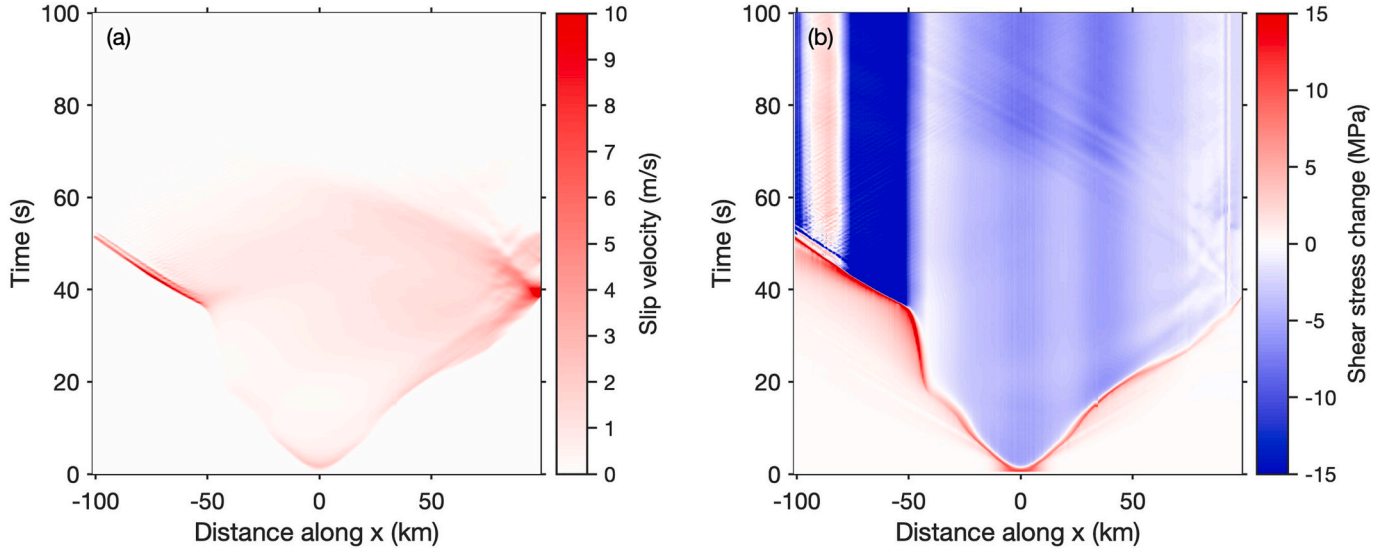

Fig. 8. The space-time plots of slip velocity and shear stress change are shown for a cross section at $y = 0$. The colour is saturated. (For interpretation of the references to colour in this figure legend, the reader is referred to the web version of this article.)

has been made to fit the rupture times of SMGAs in Kurahashi and Irikura (2013), as in Galvez et al. (2019). Galvez et al. (2019) used small asperities deeper than the elliptical zone here to match the timing of SMGAs, which probably ignored the updip rupture zone coinciding with the historic M7 earthquakes in this region (e.g., Uchida and Bürgmann, 2021). The model here is to show that a regular rupture in the central part of the fault, a slow rupture in the northern Japan Trench, and large local stress drop at deep asperities can largely explain the geodetic and tsunami observations of the 2011 Tohoku-Oki earthquake. Strong ground motion and high-rate GPS data can be examined in the future to further improve the model.

The final slip, rupture time contours every 10 s, and final shear stress change on the fault are illustrated in Fig. 9. An approximately 200 km × 200 km zone of large slip is seen off Miyagi Prefecture, consistent with previous studies (e.g., Iinuma et al., 2012; Satake et al., 2013, and Kubota et al., 2022). The peak slip (75.67 m) reaches near the trench around $y = 50$ km, which is caused by the northwardly increasing sediment thickness. Kubota et al. (2022) had peak slip of 53 m updip from the hypocenter; their model used a homogeneous half space. The northward slow rupture is clearly seen from the rupture time contours; the rupture velocity is ~850 m/s. The peak slip in the northern Japan Trench is ~20 m, located landward from the trench. The slip at the trench is diminishing from south to north. The slow rupture propagation and diminishing near-trench slip are caused by inelastic deformation

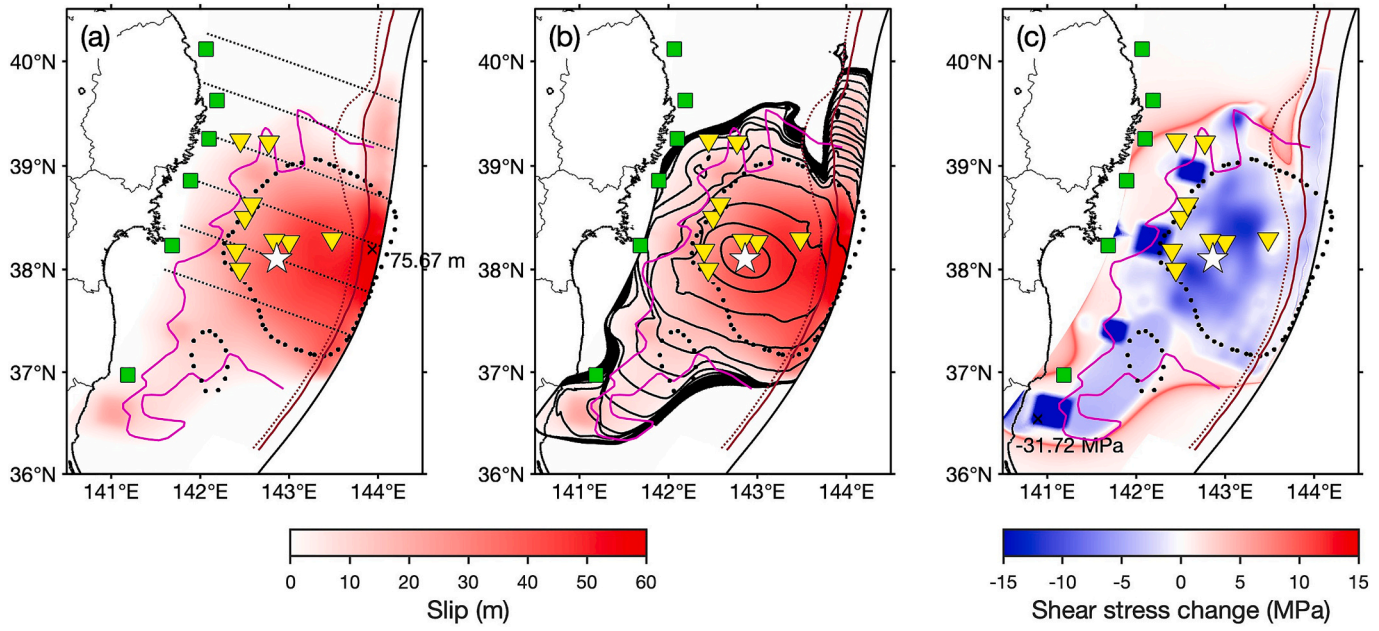

Fig. 9. The distributions of final slip, rupture time contours every 10 s, and shear stress change are mapped on the fault for the inelastic model. The colour is saturated. Large shallow slip (>50 m) occurs in the central zone extending ~200 km along trench. The slip in the northern Japan Trench is significantly less than the central part of the fault. The slow rupture velocity (~850 m/s), diminishing near-trench slip, and small stress drop (<3 MPa) in the northern Japan Trench can be clearly seen. The rupture velocity in other parts of the fault is ~3 km/s. The x symbol in (a) and (c) shows the locations of peak slip and shear stress change along with the amplitudes, respectively. Large localized slip at 4 SMGAs are associated with large shear stress changes. The dotted lines in (a) show the locations of cross sections shown in Fig. 14. (For interpretation of the references to colour in this figure legend, the reader is referred to the web version of this article.)

(shown below). The southwestward extension of the slip zone and large localized slip at the 4 SGMAs are also clearly seen, which is not in previous slip models (e.g., Iinuma et al., 2012; Satake et al., 2013; Kubota et al., 2022). Shear stress change in the central part near the hypocenter and SMGAs are large. Near-trench stress change is very small, <~3 MPa. These stress changes differ somewhat from the values used in the input of the model because there is significant normal stress reduction on the fault (less compressive) due to the free surface and material heterogeneities. Inelastic deformation also reduces the stress drop on the fault in the northern Japan Trench.

This model provides a good fit to the GPS data on land (Fig. 10), indicating the overall rupture area and slip amplitude are relatively well resolved. The deep SMGAs also affect the GPS data significantly. Due to their proximity to the coast, they are effective in causing land subsidence. The fit to the GPS is better than that of Kubota et al. (2022) due to the inclusion of the southwestward extension of the rupture and the SMGAs. However, the subsidence inland in Fukushima and Ibaraki seems overestimated, indicating that the stress drop at SMGA5 may be too large or its location is too close to the coast. No tuning of the stress drops at the 4 SMGAs of Kurahashi and Irikura (2013) is made. The fits at the 7 seafloor GPS stations are slightly worse. The overall horizontal displacements are overestimated. The uplift at GJT3 and subsidence at MYGW are underestimated. However, these offshore GPS data include several months of pre- and post-seismic deformation (Sato et al., 2011). No effort has been made to improve the fit due to the imperfect knowledge of fault geometry, material structure, and fault friction, yet the fit of this forward model seems better than some kinematic slip models from inversion (e.g., Yue and Lay, 2013; Yamazaki et al., 2018). The peak horizontal displacement (along x) reaches 65.95 m near the trench around $y = 50$ km, which is consistent with the differential bathymetry data at MY102, indicating ~69 m horizontal displacement. The peak uplift is 13.68 m at about the same location. A ~ 15 km wide large uplift zone near the trench, coinciding with the location of sediments, suggests the amplification of shallow slip by the sediment (Ma and Beroza, 2008), shown in Fig. 9a. The 10° dipping fault segment may also contribute to this amplification effect as the width of the dipping segment seems to increase towards the north. In the northern Japan Trench, the large uplift still exists despite diminishing shallow slip, due to inelastic deformation.

Fig. 11 compares a snapshot of slip velocity, shear stress change, and seafloor displacements between the inelastic model and an elastic model. The detailed rupture process of the elastic model is shown in Movie S2. The peak rate reaches 9.54 m/s in the elastic model compared to 1.91 m/s in the inelastic model in the northern Japan trench at 122 s. The rupture velocity is also faster in the elastic model. The fast-moving rupture in the elastic model produces significantly larger horizontal displacement than that in the slowly moving rupture of the inelastic model. The inelastic strain develops in the outer wedge, which significantly reduces horizontal displacement but increases uplift. The shear stress change is also greater in the elastic case due to larger slip on the fault.

The final slip, rupture time contours, and shear stress change in the elastic model are illustrated in Fig. 12. The results are nearly identical to the inelastic model except in the shallow region north of ~38.5°N, which is due to small *CF* values south of ~38.5°N in the inelastic model. Larger shallow slip and faster rupture velocity north of ~38.5°N are clearly seen. The rupture also propagates farther to ~40.4°N. The slip peaks at the trench. The rupture velocity is less but close to the shear

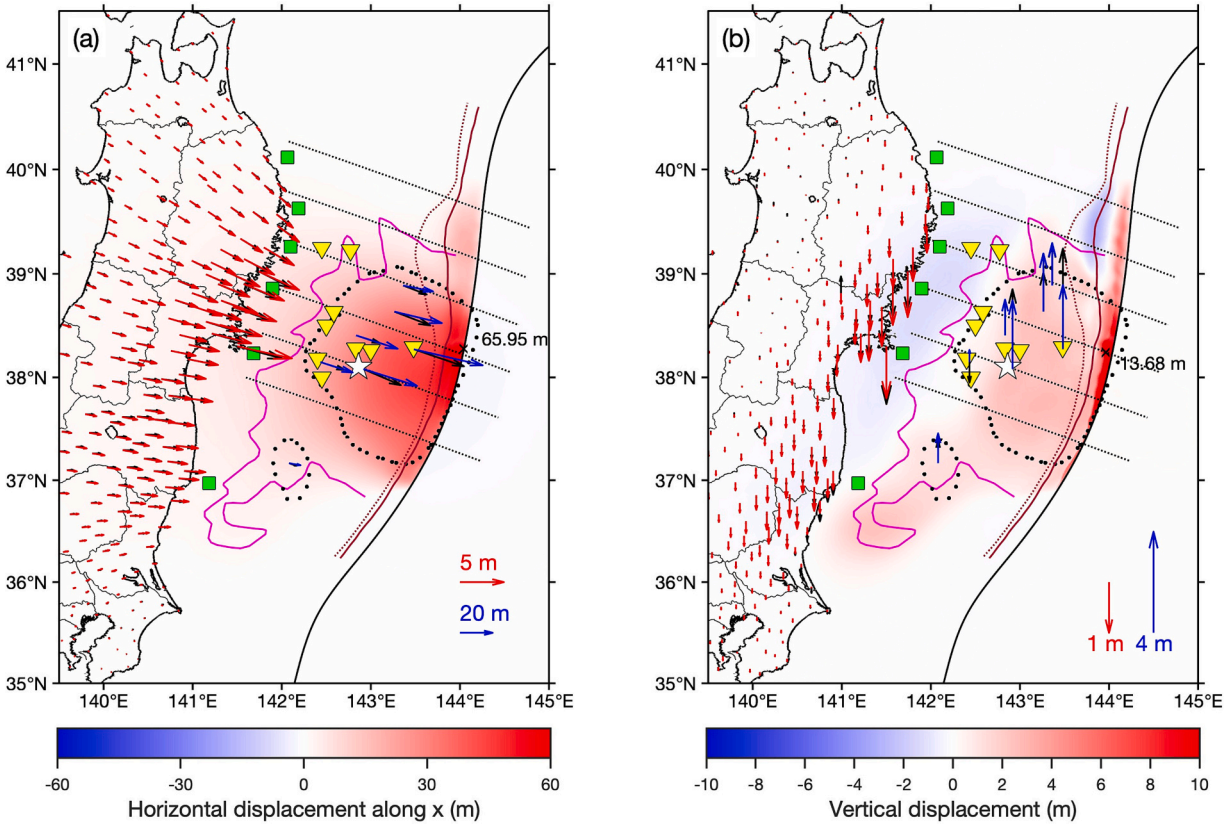

Fig. 10. The distributions of horizontal and vertical surface displacements and the comparisons with on- and off-shore GPS data are shown for the inelastic model. The colour is saturated. The data is in black. The synthetic on-shore GPS vectors are in red and off-shore in blue. The x symbol denotes the peak displacement location in each panel. Note the different scales of displacement vectors on- and off-shore. The dotted lines show the locations of cross sections shown in Fig. 14. Both the peak horizontal and vertical displacements in the northern Japan Trench are located landward from the trench in contrast to the central slip zone. (For interpretation of the references to colour in this figure legend, the reader is referred to the web version of this article.)

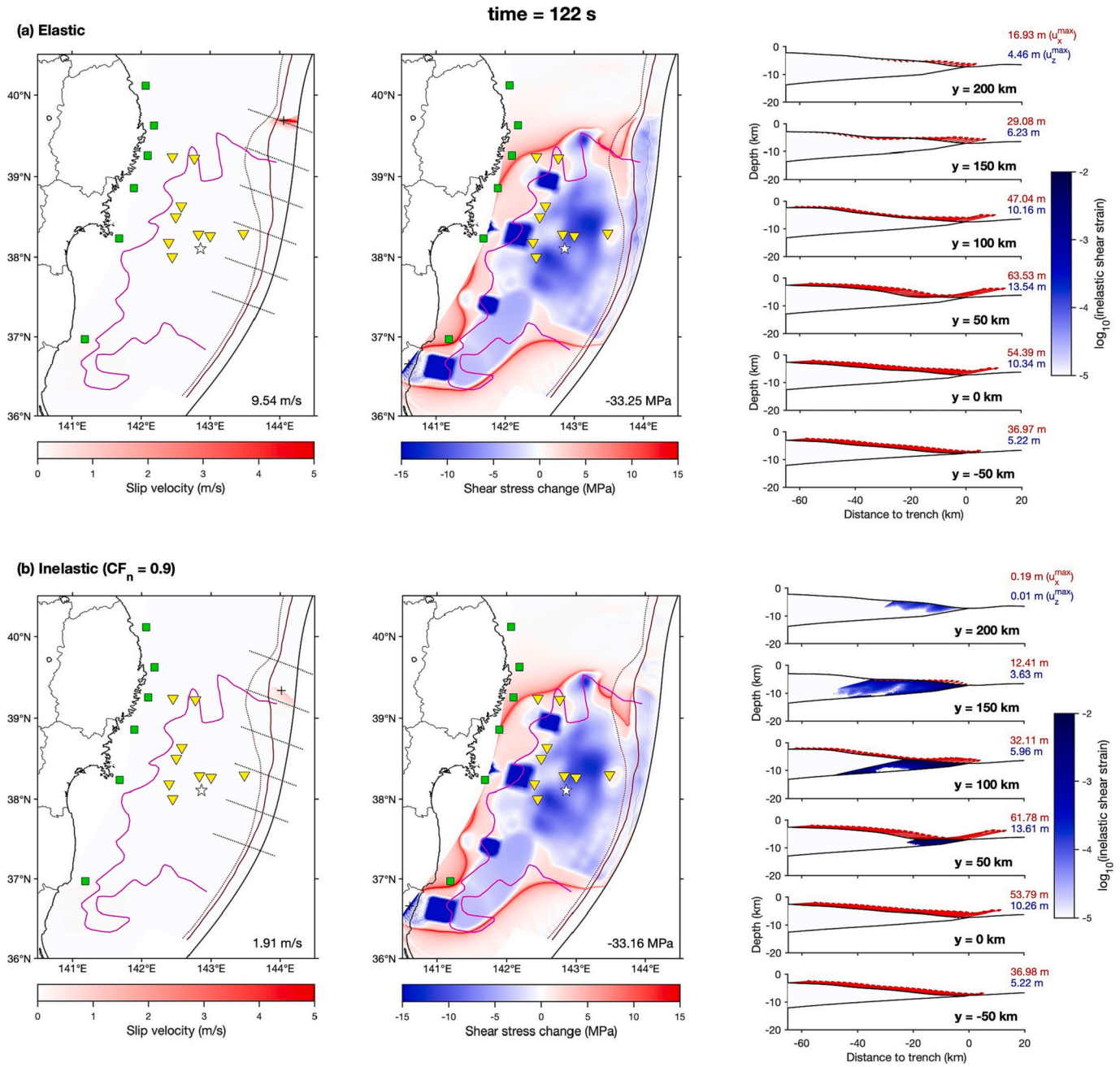

Fig. 11. Snapshots of slip velocity, shear stress change, and surface displacement vectors at 6 cross sections for (a) elastic and (b) inelastic models at 122 s are compared. The peak value (the + symbol denotes the location) is shown in the lower right of two left panels. The peak amplitudes of horizontal and vertical displacements at each cross section are shown on the right panel in red and blue, respectively. The locations of cross sections are shown in the left panel. In (b) the inelastic shear strain in the wedge is also shown. The two models are nearly identical except for in the northern Japan Trench. The rupture in the northern Japan Trench in the elastic model is faster with larger slip rate (9.54 m/s), producing larger horizontal displacement at the trench. The slip rate in the inelastic model is much less (1.91 m/s) and the horizontal displacement in the northern Japan Trench is reduced by inelastic deformation. (For interpretation of the references to colour in this figure legend, the reader is referred to the web version of this article.)

wave speed of the sediment (1500 m/s) compared to ~850 m/s in the inelastic case. The dynamics of shallow rupture and seafloor displacement in the elastic model (Figs. 11a and 12) can be largely attributed to the constructive interference of the free surface and compliant hanging wall (Ma and Beroza, 2008).

The fit to the GPS data is nearly identical to the inelastic model (Fig. 13), indicating that GPS data does not have good resolution to the near-trench slip in the northern Japan Trench. Large horizontal and vertical seafloor displacements are due to large slip peaking at the trench, which is illustrated in cross sections in comparison with the inelastic model in Fig. 14. Large discontinuities of displacements across the trench can be seen in the elastic model, while in the inelastic model the slip and horizontal displacement are significantly smaller, and the discontinuity is more subdued at the trench. Although the absolute uplift is larger in the elastic model the peak slip is also several times larger. The peak uplift at $y = 150$ km and $y = 200$ km are comparable between the two models; if the peak uplift scaled by the slip denotes the efficiency of producing uplift the efficiency of inelastic deformation is several times larger than that of slip on the fault. This is similar to the results of previous work (e.g., Ma, 2012; Ma and Hirakawa, 2013; Ma and Nie,

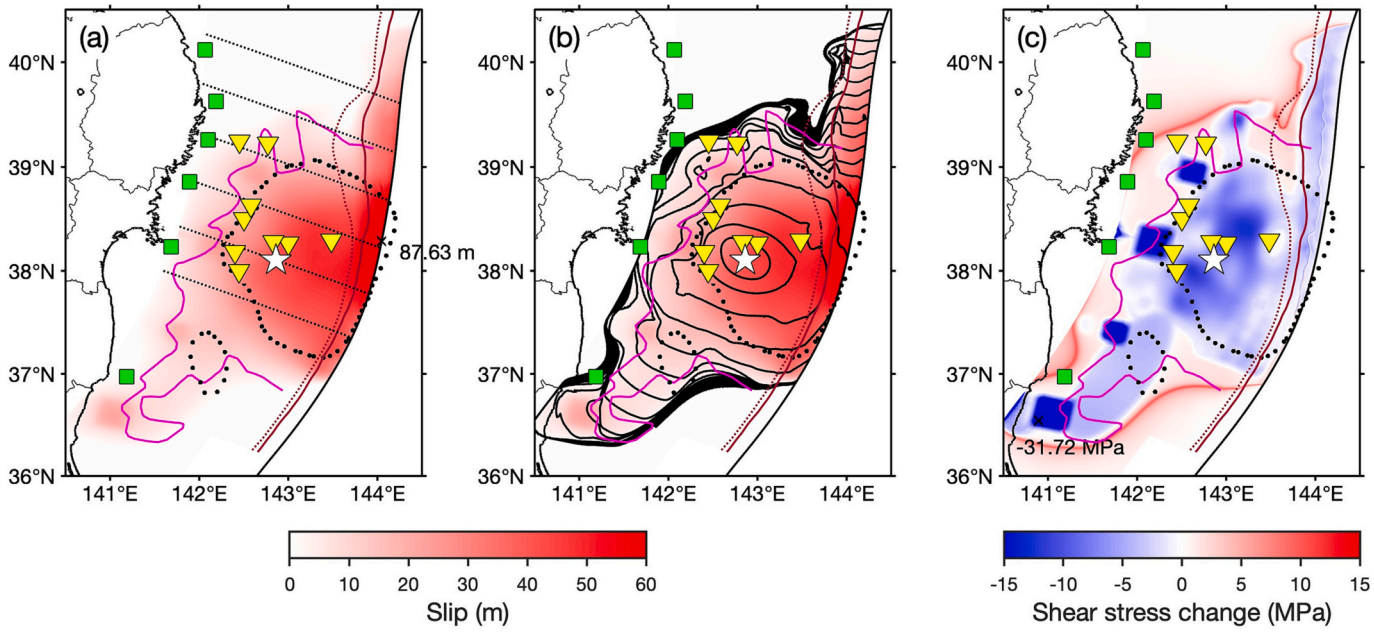

Fig. 12. Similar to Fig. 9 but for an elastic model. The rupture velocity in the northern Japan Trench is much faster than in the inelastic model although the sediment is thick. The stress drop and slip (peaking at trench) in the northern Japan Trench are also larger. (For interpretation of the references to colour in this figure legend, the reader is referred to the web version of this article.)

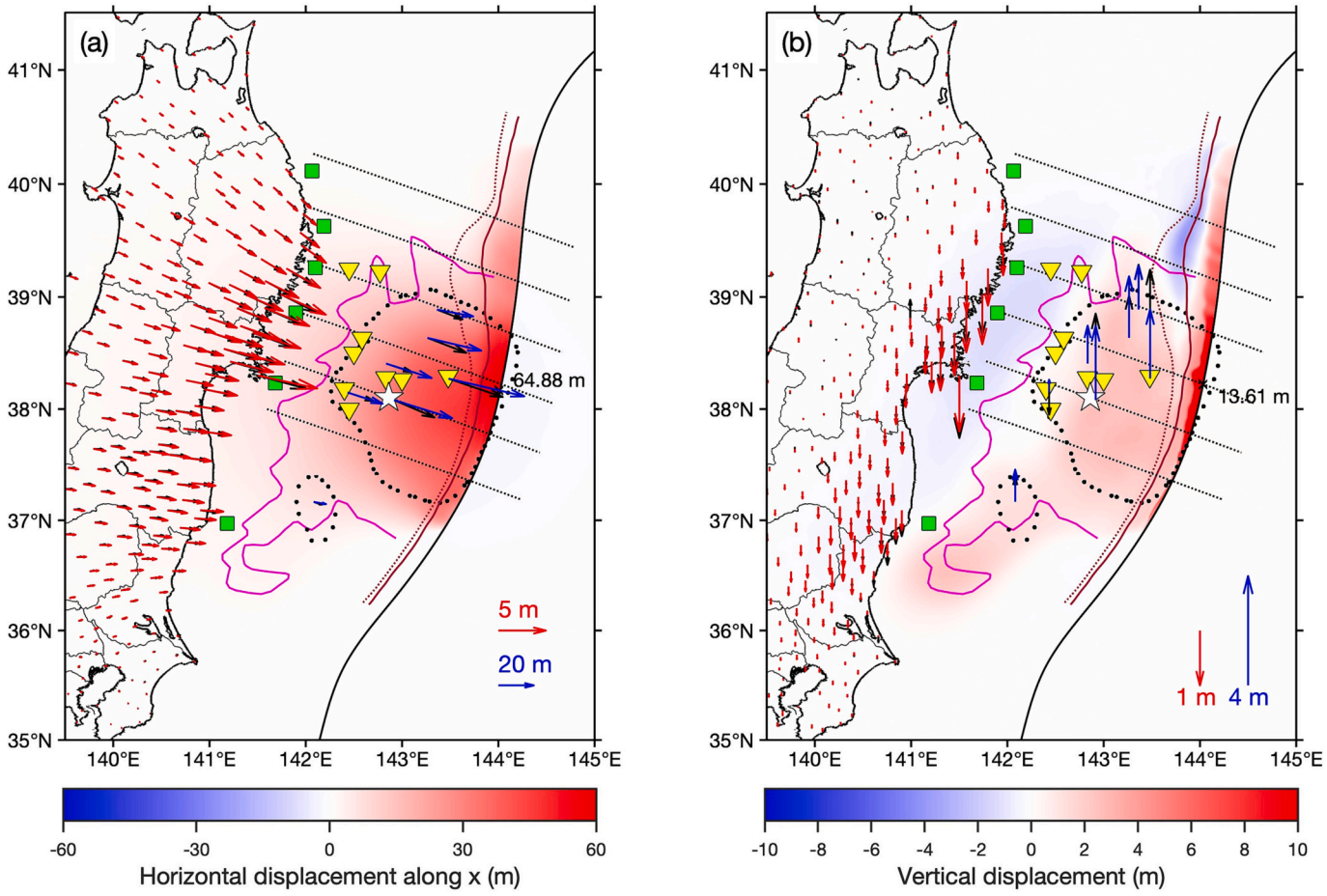

Fig. 13. Similar to Fig. 10 but for an elastic model. In the northern Japan Trench both horizontal and vertical displacements are larger than in the inelastic model and peak at the trench due to large trench slip (inconsistent with the differential bathymetry observations). A nearly identical fit to the on- and off-shore GPS data is obtained, indicating no resolution of data to the slip in the northern Japan Trench. (For interpretation of the references to colour in this figure legend, the reader is referred to the web version of this article.)

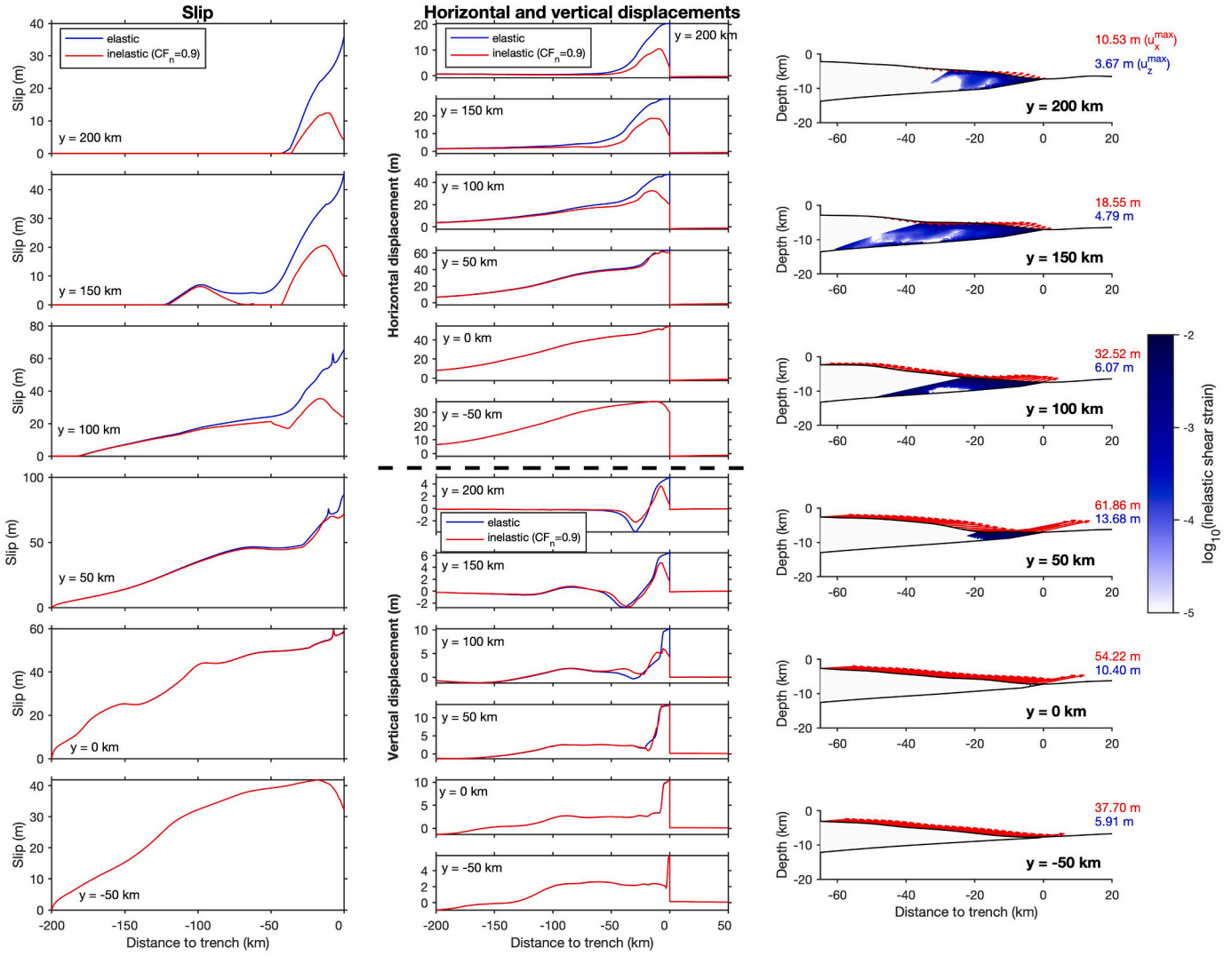

Fig. 14. Comparisons of final slip and surface displacements at 6 cross sections between the elastic and inelastic models are shown. The inelastic strain and surface displacement vectors at the cross sections in the inelastic model are shown on the right, where the peak amplitudes of horizontal and vertical displacements are shown in red and blue, respectively. The reduction of shallow slip and horizontal displacement in the northern Japan Trench is clearly seen. The vertical displacement is only mildly reduced by the diminishing slip because the inelastic deformation increases the uplift. The seafloor displacement pattern in the inelastic model is much more consistent with the differential bathymetry observations (Fig. 1) than the elastic model. (For interpretation of the references to colour in this figure legend, the reader is referred to the web version of this article.)

2019; Wilson and Ma, 2021) although the shallow slip here is not completely diminished due to >50 m slip in the south. The overall horizontal and vertical displacements near the trench in the inelastic model are much more consistent with the differential bathymetry observations in the northern Japan Trench shown in Fig. 1.

The total potency on the fault in the inelastic model is 1.3858×10^{12} m^3. The total potency in the wedge is 3.4462×10^{10} m^3, which is only 2.49% of the total potency on the fault because the potency release is dominated by the large slip south of ~38.5°N. The total potency of this model is 1.4203×10^{12} m^3, which give rise to moment magnitude M_W 9.10 assuming a shear modulus 40 GPa. The total potency of the elastic model is 1.5176×10^{12} m^3, corresponding to M_W 9.12. The potency rate on the fault and in the wedge for both elastic and inelastic models are shown in Fig. 15. The total rupture durations in both models are ~200 s, with slightly longer rupture duration in the inelastic model despite shorter rupture distance. The first peak in the potency-rate time histories is from the large slip associated with rupture breakout at the trench and the second peak is associated with the large stress drop at SMGA5. However, after the first peak the potency rate in the elastic model is consistently higher than in the inelastic model, which is due to large shallow slip in the northern Japan Trench in the elastic model. The potency rate function in the wedge peaks at about the same time as the large rupture breakout phase due to inelastic deformation caused by large dynamic stress change associated with large shallow slip. After the first peak the potency rate in the wedge is barely recognizable in this figure due to slow rupture propagation, but the potency release in the wedge plays a fundamental role in tsunami generation and diminishing slip, as was shown above.

The two dynamic rupture models are also tested by using the observed tsunami waveforms. I use a staggered-grid finite-difference tsunami code, same as in Du et al. (2021), to solve a 2D nonlinear Boussinesq equation using a realistic bathymetry and topography on a uniform grid of 1350 m. The time-dependent seafloor displacements from the dynamic rupture model are used to generate the tsunami. At each time step, the contribution of horizontal displacement in the tsunami generation is calculated by

$$u_h = u_x \frac{\partial D}{\partial x} + u_y \frac{\partial D}{\partial y}, \tag{12}$$

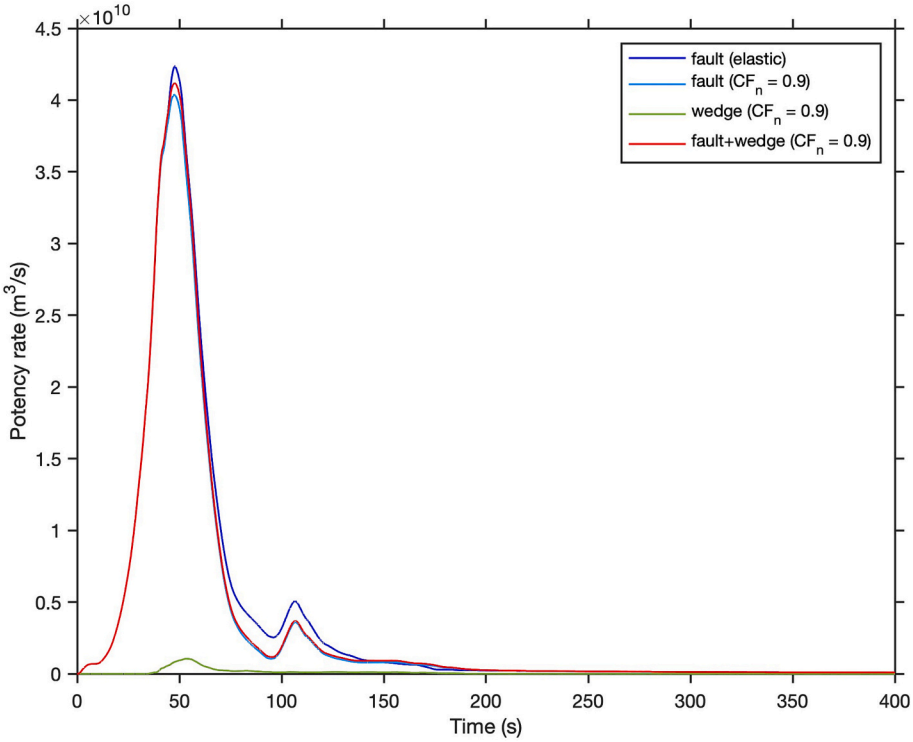

Fig. 15. The potency rate time histories are compared between the elastic and inelastic models. The difference between blue and red curves after the first peak is due to the different rupture characteristics in the northern Japan Trench. (For interpretation of the references to colour in this figure legend, the reader is referred to the web version of this article.)

where u_x and u_y are two horizontal displacement components at each time step and D (positive downward) is ocean depth (Tanioka and Satake, 1996). The total seafloor uplift relevant to tsunami generation is

$$u_{ts} = u_h + u_z, \tag{13}$$

where u_z is vertical displacement. A lowpass Kajiura filter (Kajiura, 1963) with a cutoff wavelength of 6 km is applied (same as in Kubota et al., 2022) before entering u_{ts} in the continuity equation of the tsunami equation because any shorter-wavelength components than ocean depth are naturally filtered out by the ocean. The tsunami simulations are run for a total duration of 2 h with time step of 2 s.

Figs. 16 and 17 show how this is done in the inelastic model at $t =$ 480 s. The horizontal displacement makes a significant contribution to u_h especially when the seafloor is steep (within ~100 km from trench). In the continental shelf the contribution to u_h is negligible because the seafloor is nearly flat. The contribution from the horizontal

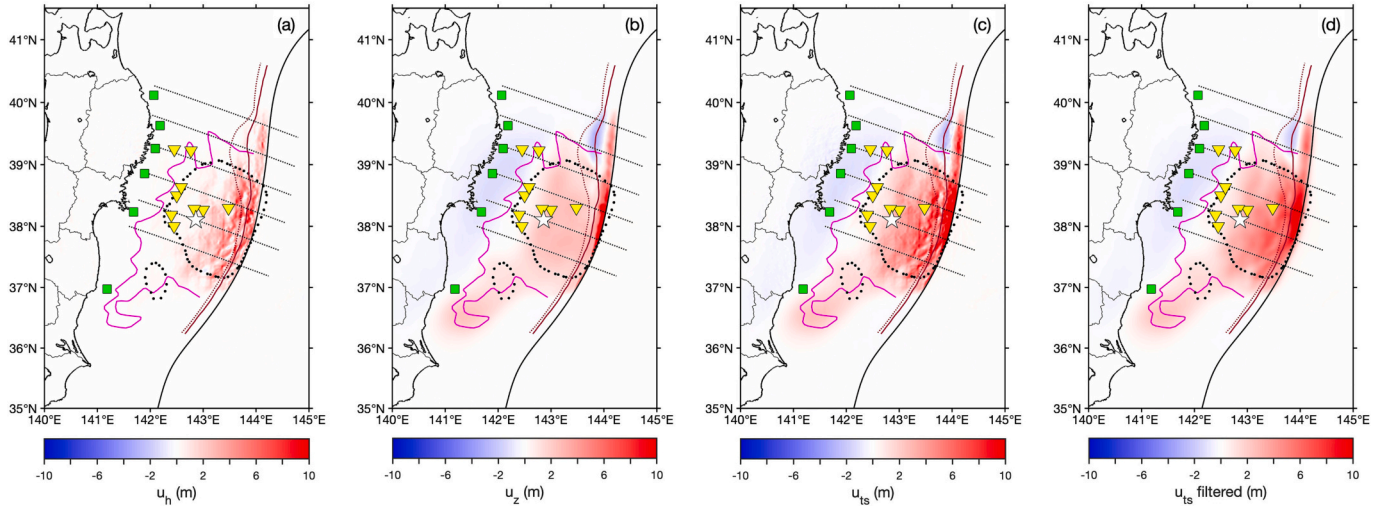

Fig. 16. The distributions of different contributions to sea surface height in the inelastic model at 480 s are mapped at the surface: (a) contribution of horizontal displacement, u_h, (b) vertical displacement, u_z, (c) $u_{ts} = u_h + u_z$, and (d) u_{ts} lowpass-filtered with a 6 km cutoff wavelength. The dotted lines show the locations of cross sections shown in Fig. 17. In (d) the broad uplift off Miyagi and short-wavelength uplift of similar amplitude in the northern Japan Trench can be clearly seen. The short-wavelength uplift zone in the northern Japan Trench is the source of impulsive tsunami observed offshore the Sanriku coast in 2011, which is mostly due to inelastic wedge deformation. The horizontal displacement contributes to sea surface height more significantly in the central large slip region than in the northern Japan Trench. (For interpretation of the references to colour in this figure legend, the reader is referred to the web version of this article.)

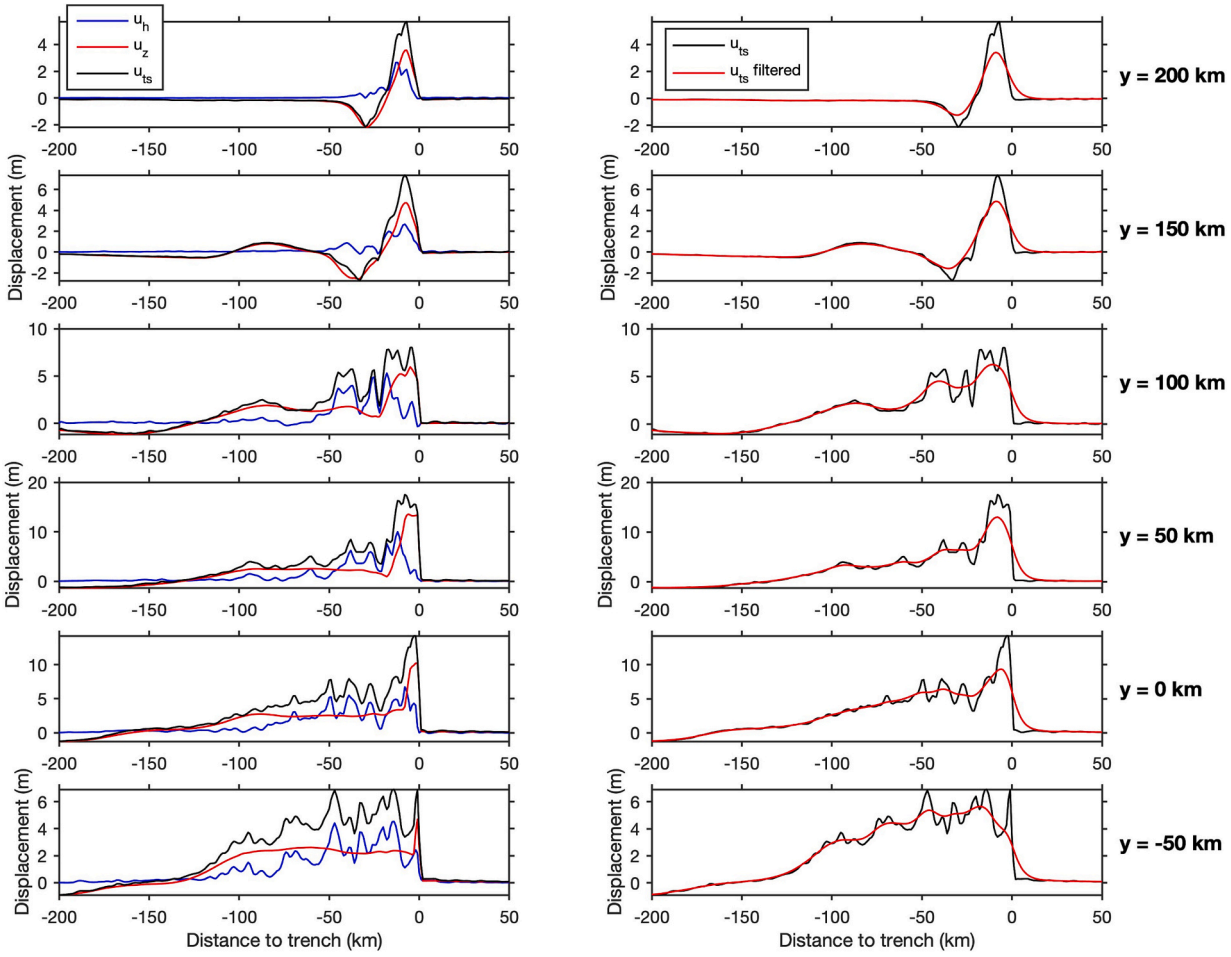

Fig. 17. The distributions of different contributions to the sea surface height in the inelastic model at 480 s are plotted at 6 cross sections. The relative contributions can be clearly seen. The contribution of horizontal displacement to sea surface height is much greater off Miyagi where the slip is large and the fault is wide. In the northern Japan Trench, the horizontal displacement diminished by inelastic deformation plays a less significant role and most of the contributions to tsunami generation is from the inelastic uplift. (For interpretation of the references to colour in this figure legend, the reader is referred to the web version of this article.)

displacement u_h exceeds u_z in the central region where slip is large, fault dip is shallow, and bathymetry is steep. After the filtering of short-wavelength variations u_h is still larger than u_z in a large region of the seafloor. However, north of ~38.5° it shows a different picture. Inelastic deformation diminishes shallow slip and horizontal displacement, thus u_h becomes less significant. The major contribution to u_{ts} is the vertical displacement, especially after the lowpass filtering (see cross sections at $y = 150$ km and 200 km in Fig. 17). Figs. S3 and 4 show a slightly larger contribution of u_h north of ~38.5°N in the elastic model (inconsistent with the observations in Fig. 1b); however, the larger contribution of u_h is mostly seen in the central region where large slip occurs.

The comparison between the simulated and observed tsunami waveforms at GPS buoys and OBP stations for the inelastic model is shown in Fig. 18. The impulsive signal recorded at stations TM1, TM2, 802, 804, and 807 off the Sanriku coast are remarkably consistent with the data in terms of amplitude, width, and arrival time. The model underestimates the broad signal before the arrival of the impulsive signal at TM1, probably because the seafloor uplift near TM1 is underestimated. The impulsive signal off the Sanriku coast is mostly caused by the inelastic wedge deformation north of 39°N. The consistency with the data confirms that the inelastic deformation and slow rupture velocity can explain the large tsunami generation in the northern Japan trench. The fit to the station 21418 is nearly perfect. This station is located at about the similar latitude with the inelastic deformation zone but in the deep ocean, which places a tight constraint on the rupture time and width and amplitude of the uplift, again confirming the inelastic deformation model but from a different direction. The elastic model overestimates the amplitude of the impulsive signal off Sanriku coast and at station 21418 (Fig. S5). The arrival of the impulsive tsunami from the elastic model is also too fast, likely due to the fast rupture velocity in the north. The more detailed comparisons of elastic and inelastic models with data at stations TM1, TM2, 802, 804, 807, and 21418 are illustrated in Fig. 19, showing the differences in tsunami that these two models generate.

Both the elastic and inelastic models produce similar tsunami waveforms at other stations because the two models differ mostly only in the northern Japan Trench. The simulated waveforms also show good consistency with the data. Excellent fit is seen at 3 OBP stations seaward from hypocenter (P08, P09, and GJT3), capturing the initial increase and large decrease in the ocean bottom pressure. The large decrease in the data places a tight constraint on the seafloor uplift at the 3 stations. Note that at GJT3 the models can explain the tsunami data well, but underestimate the uplift in the seafloor GPS data (Figs. 10 and 13), indicating that the GPS data probably does include some non-coseismic signals. The large pressure decrease, however, is overestimated at 4 stations landward from the epicenter, indicating the subsidence is underestimated (as can be seen in MIYW in Fig. 10). However, the overall waveform is fit well, but with a constant offset. The displacements at these four stations are strongly affected by the SMGA1 as well as the SMGA2 in the downdip direction. The large local slip at these two asperities pushes the seafloor up in the updip direction, which may cause the underestimation of the subsidence at these stations, suggesting that

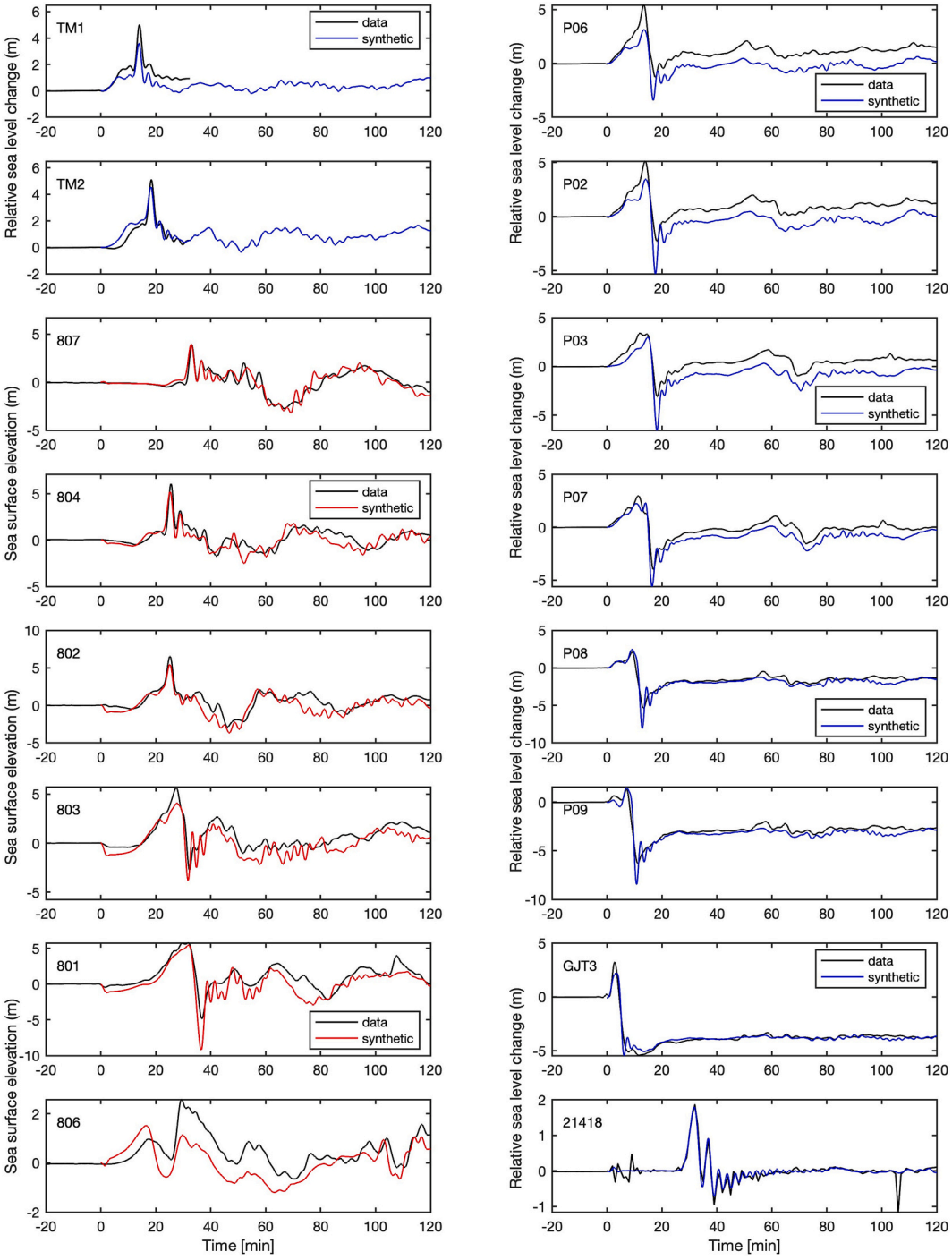

Fig. 18. Comparisons of the synthetic and observed tsunami waveforms are shown for the inelastic model. The data is in black. The synthetic waveforms at GPS buoys and OBP stations are in red and blue, respectively. The OBP time histories show the relative displacement between sea surface and seafloor. All the waveforms are lowpass-filtered at 150 s. The amplitude, width, and arrival time of the impulsive tsunami at stations TM1, TM2, 807, 804, and 802 are consistent with the data, indicating a good resolution of the rupture velocity and seafloor displacements in the northern Japan Trench. The broad signal before the arrival of impulsive tsunami at TM1 indicates that the seafloor uplift near the station is underestimated. The fit at the DART 21418 tightly constrains the rupture velocity and deformation in the northern Japan Trench. The fit at other stations are also good. See text for more discussions. Around $t = 0$ the data at GPS buoys show a minimal sea surface drop less than in the synthetics and subsidence in the on-land GPS data, which may be due to data processing. No amplitude offset is applied to the waveforms, unlike in some studies (e.g., Yamazaki et al., 2018). (For interpretation of the references to colour in this figure legend, the reader is referred to the web version of this article.)

the stress drop may be too large and/or their locations may be slightly mislocated. Similarly, the first peak at station 806 is overestimated, which is probably due to the SMGA5. The SMGAs contributes to the land subsidence effectively, which explains why the fit to the on-land GPS data is better than in Kubota et al. (2022). In this model no effort is made to improve the fit. Future improvements of the model may be able to explain the OBP and on-land GPS data better together with strong ground motion and high-rate GPS data when better plate geometry, material properties, stress drop, and constraints on the SMGAs become available.

Movie S3 shows the tsunami generation and propagation produced by the time-dependent seafloor deformation of the inelastic model more

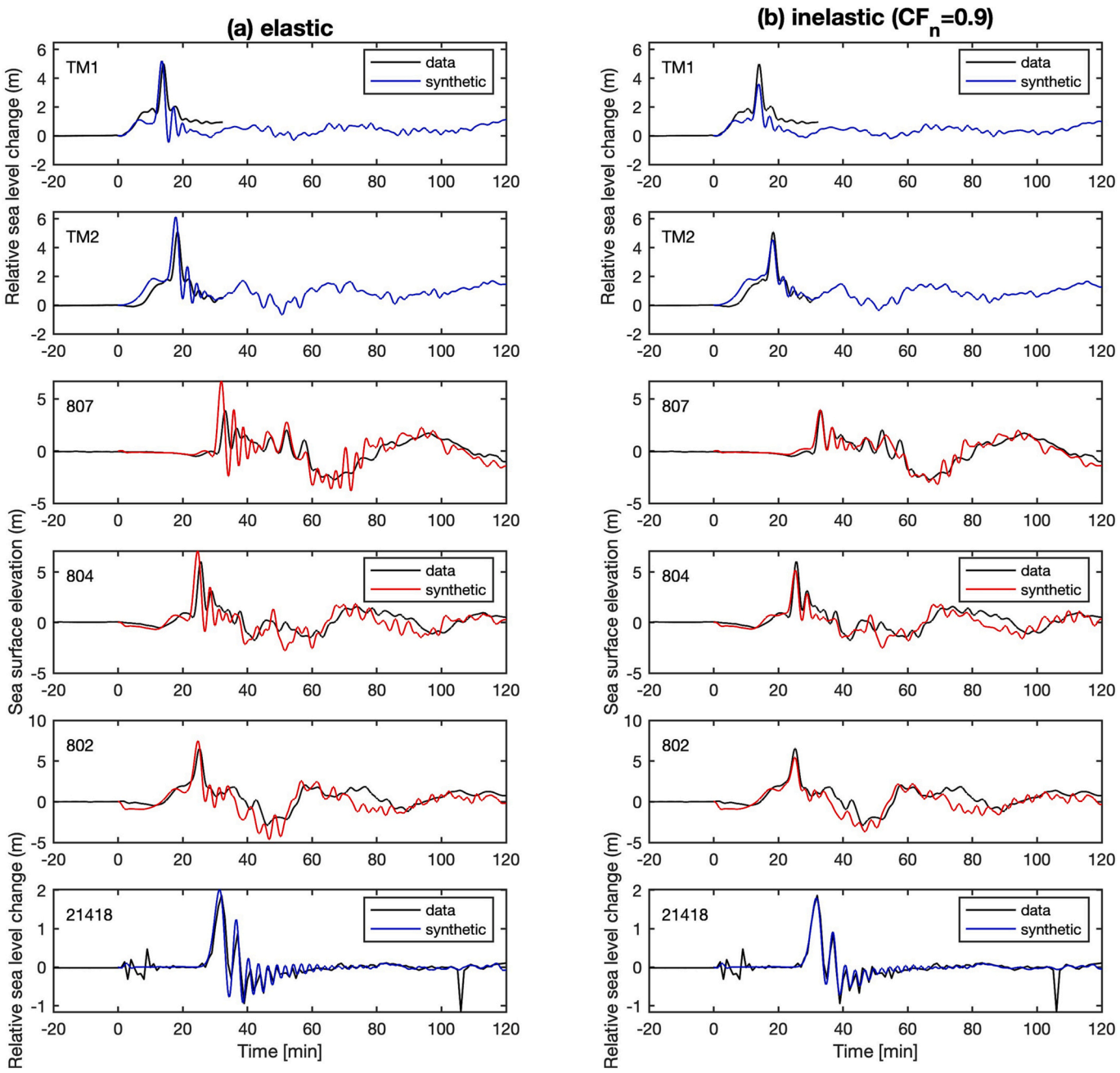

Fig. 19. Detailed comparison of synthetic tsunami waveforms with data at TM1, TM2, three GPS buoys off the Sanriku coast, and DART 21418 for (a) elastic model and (b) inelastic model. Elastic model produces impulsive tsunami with earlier arrival and larger amplitude than the offshore data and overpredicts the amplitude at DART 21418. The amplitude and timing of the impulsive tsunami are well predicted by the inelastic model. (For interpretation of the references to colour in this figure legend, the reader is referred to the web version of this article.)

clearly. The long-wavelength tsunami by the broad uplift above the large slip zone off Miyagi Prefecture and short-wavelength tsunami originated from the northern Japan Trench off Iwate Prefecture can be clearly seen. The tsunami wavelengths decrease while the amplitudes increase during the shoaling process. A stronger shoaling process can be seen in the short-wavelength tsunami in the north, which propagates slowly and originates from near deep trench far from the shore, so it experiences a longer shoaling process during which the amplitude increases significantly. When this short-wavelength tsunami passes TM1, TM2, and 3 GPS buoy stations in the north (807, 804, and 802) it produces an impulsive signal as observed at these stations. This impulsive tsunami is seen to produce a large impact on the rugged Sanriku coast north of 39°N, which can probably explain the mysterious large runup observed in Iwate Prefecture ((Du et al., 2021). The long-wavelength tsunami produces large impact mostly south of 39°N, such as along southern Sanriku coast and in Ishinomaki – Sendai Plain. Off Fukushima, the initial tsunami is due to the slip close to the coast, which gives the first peak recorded at GPS buoy 806. The second peak in the record is from the diffracted wave from the central uplift zone, as shown in the movie. The dispersive tsunami propagating into the deep ocean can also be clearly seen, which was recorded by the station 21418. It may be worth pointing out that a non-dispersive tsunami model was used by Satake et al. (2013). To fit the dispersive data, such as at station 21418, their model may have included some unphysical slip features.

4. Discussion

The minimalist dynamic rupture model presented here likely provides a more complete and self-consistent picture of the 2011 Tohoku-Oki earthquake and tsunami than previous kinematic slip models. Three major zones with different rupture characteristics can be identified: (1) a central zone of large shallow slip >50 m off Miyagi Prefecture, (2) a southwestward zone of small slip off Fukushima Prefecture, and (3) a northern rupture zone up to 39.8°N off Iwate Prefecture with slow rupture velocity, efficient tsunamigenesis, and diminishing shallow slip. In zones 1 and 2 there are deep asperities near the down-dip edge of rupture area generating strong ground motion. The broad uplift in zone 1 is essential in explaining the large tsunami inundation distances in Miyagi Prefecture, such as Ishinomaki-Sendai Plain, but the runup there is not large (e.g., Saito et al., 2014), as well as the large tsunami in southern Sanriku coast, such as in Kesennuma, Minami-Sanriku, and Onagawa. Zone 2 mainly contributes to the initial rise of tsunami off Fukushima Prefecture. Zone 3 is crucial in explaining the mysterious large tsunami (up to 40 m) along the Sanriku coast north of 39°N, which is likely due to the amplification of short-wavelength (impulsive) tsunami by the rugged Sanriku coast (e.g., Du et al., 2021). Zone 3 is also where the 1896 Sanriku earthquake occurred (see Fig. 2). Kanamori (1972) identified this earthquake as a tsunami earthquake, which generates large tsunami but radiates weak high-frequency energy. The inelastic deformation of thick sediment in the northern Japan Trench provides a self-consistent explanation to these anomalous characteristics of a tsunami earthquake and may also explain why this northern rupture zone was not resolved in the inversions of strong ground motion and teleseismic data for the 2011 Tohoku-Oki earthquake (e.g., Lay, 2018) because of depletion in high-frequency radiation due to plastic energy dissipation (Ma and Hirakawa, 2013). The geodetic data also lacks resolution to the slip and inelastic deformation in zone 3 as shown in both the elastic and inelastic models here, which is probably why geodetic inversions (e.g., Iinuma et al., 2012) also failed to resolve this zone.

The inelastic deformation model presented here may seem different from the previous models by Ma and Nie (2019). Ma and Nie (2019) considered a M_W 8 earthquake with a planar fault and constant fault width and showed that near-trench slip can be completely diminished when *CF* is large. However, in this model the slip in the northern Japan Trench is not completely diminished, somewhat consistent with the differential bathymetry data, although peak slip and uplift are landward from trench. This is because there is a significant difference in fault width along strike in this model. In zone 1, the fault width is ~200 km, which produces large shallow slip >50 m at the trench, enhanced by the free surface and wedge sediment. However, in zone 3, the fault width is only <50 km. Inelastic wedge deformation is unlikely to reduce >50 m slip abruptly to zero at trench while maintaining a propagating rupture on such a narrow fault. Also, the velocity-strengthening friction is not used in zone 3. The completely diminishing near-trench slip with significant inelastic wedge deformation is still a plausible scenario in considering large tsunamigenesis when such large fault-width variations are not present, such as in the 1896 Sanriku earthquake, or there are shallow velocity-strengthening frictional behaviors on the fault.

It may be fundamentally flawed to use elastic dislocation models in explaining tsunami generation in sediment-rich margins, as the differential bathymetry observations in the northern Japan Trench and mysterious large tsunami runup along the Sanriku coast north of 39°N showed (Fig. 1). In order to explain tsunamigenesis by interplate earthquakes, elastic dislocation locations invariably resort to large shallow slip (e.g., Satake and Tanioka, 1999; Satake et al., 2013; Yamazaki et al., 2018; Sallarès and Ranero, 2019; Cheung et al., 2021; Fujii et al., 2021). However, the applicability of elastic dislocation theory in shallow sediment-rich margins is questionable, which probably explains why the elastic dislocation models failed to explain the key observations in the 2011 Tohoku-Oki earthquake and tsunami discussed here. The reader is refered to Wilson and Ma (2021) for more detailed discussions of the applicability of elastic dislocation theory.

It is important to realize that the efficiency of generating uplift (i.e., uplift scaled by slip) is largely limited by the sum of surface slope (α) and fault dip (β) at the trench, $\alpha+\beta$, in an elastic dislocation model. On a shallowly dipping fault this efficiency can be quite low because α is comparable to β once small-wavelength steep bathymetric features are filtered out (Kajiura, 1963), Although >50 m slip at the trench indeed generated a large tsunami the efficiency of generating tsunami is low. However, for inelastic deformation the efficiency of generating uplift is much higher. That greater efficiency can be understood by viewing the inelastic deformation as a continuum representation of frictional sliding on steeply dipping microfractures generated by dynamic stress. By looking at the near-trench slip and u_{ts} distributions (Figs. 9 and 16) the difference in the efficiencies of generating uplift off Miyagi and Iwate Prefectures may be evident. In explaining exceptionally large tsunamigenesis of tsunami earthquakes and events like the 2004 Sumatra earthquake and the 2011 Tohoku-Oki earthquake maybe an efficient tsunami generation mechanism is preferred.

An early idea to explain the large tsunamigenesis of tsunami earthquakes is that these earthquakes rupture to the shallowest reach of the subduction margin where there can be thick sediments (e.g., Okal, 1988; Satake and Tanioka, 1999; Polet and Kanamori, 2000). The argument is simply by the definition of seismic moment $M=\mu SA$, where μ is shear rigidity, S is average slip, and A is fault area. If the moment is held constant the low rigidity of sediments inevitably increases shallow slip, which increases seafloor deformation in leading to large tsunamigenesis. This simple hypothesis falls within the realm of elastic dislocation theory, which identified the importance of sediment, but its physical interpretation may not be correct. As shown here, large tsunamigenesis in the northern Japan Trench can be due to inelastic deformation of sediment by weak strength, instead of low rigidity. The low rigidity of sediments does increase shallow slip in the elastic model in this work, which, however, is inconsistent with the differential bathymetry observations in the northern Japan Trench.

In order to explain the deficiency in high-frequency seismic radiation and slow rupture propagation of tsunami earthquakes most models again rely on sediments (e.g., Kanamori and Kikuchi, 1993; Polet and Kanamori, 2000; Geist and Bilek, 2001). To explain the large tsunamigenesis of truly anomalous tsunami earthquakes, such as the 1896 Sanriku earthquake and 1946 Aleutian Unimak Islands earthquake, Kanamori and Kikuchi (1993) proposed sediment slump, but did not explain why the earthquakes were slow. For moderately anomalous tsunami earthquakes, such as the 1992 Nicaragua earthquake, a thin sedimentary layer over horst-and-graben structure due to sediment subduction was proposed (e.g., Kanamori and Kikuchi, 1993; Polet and Kanamori, 2000). The rupture reaches the shallowest depth (possibly seafloor) because the horst-and-graben structure (fault roughness) enhances fault coupling to lead to a velocity-weakening regime. The sedimentary layer cannot be too thick as it can lead to velocity-strengthening frictional behavior to stop the rupture. The low rigidity of thin sediments can lead to slow rupture propagation and gives rise to deficiency in high-frequency radiation. However, the concept of thin sediments in causing slow rupture velocity and weak seismic radiation may be intuitive but is questionable. If a thin sedimentary layer is in the fault zone the energy trapped within the fault zone by the material contrast can lead to supershear rupture; the slip-rate field is always perturbed by high-frequency oscillations due to wave reverberations in the fault zone (e.g., Harris and Day, 1997), which inevitably lead to high-frequency radiation. If a large sedimentary prism is present the rupture velocity can be controlled by the sediment (e.g., Lotto et al., 2017), as also shown in this work (Figs. 11a and 12). However, the compliant hanging wall and free surface lead to large strength drop (static friction minus dynamic friction) associated with large slip rate and near-field ground motion (e.g., Ma and Beroza, 2008), also shown in Fig. 11a, which again leads to more high-frequency radiation.

Furthermore, sediments are well known to amplify ground motion, so it seems unreasonable to conclude that elastic deformation of sediments causes weak and low-frequency radiation. Similarly, rough plate interface (i.e., horst-and-graben structures) should lead to more high-frequency radiation if the off-fault response is purely elastic.

It seems that for the above idea by Kanamori and Kikuchi (1993) and Polet and Kanamori (2000) to work significant inelastic deformation of sediments may have to be invoked. The inelastic deformation can cause slow rupture velocity, deficient high-frequency radiation, and reduced moment-scaled radiated energy because it is a large energy sink (Ma, 2012; Ma and Hirakawa, 2013). In this work, rupture velocity in the northern Japan Trench is ~850 m/s, only about half the S-wave speed in the wedge. Meanwhile, the inelastic deformation is efficient in causing tsunami, thus providing a self-consistent and possibly unifying interpretation to the anomalous characteristics of tsunami earthquakes and shallow rupture characteristics of large tsunamigenic earthquakes. The horst-and-graben structure can also induce inelastic deformation at geometric complexities of fault surface (e.g., Dunham et al., 2011), further causing slow rupture velocity and deficiency in high-frequency radiation.

It is sobering to see that the qualitative concepts of sediment leading to large slip, slow rupture velocity, and deficiency in high-frequency radiation discussed above has been widely accepted and followed by many researchers (e.g., Bilek and Lay, 1998, 1999; Geist and Bilek, 2001; Lay et al., 2012). In a recent study, Sallarès and Ranero (2019) presented a generic 1D velocity model of overriding plate by averaging worldwide controlled-source tomographic models and found a 4–5 times reduction in shear rigidity near the seafloor. They claimed that shallow modulus reduction is sufficient to explain large shallow slip, slow rupture velocity, and deficiency in high-frequency radiation in shallow subduction zones around the globe. However, as discussed above, these concepts can be over-simplified and may misinterpret the physics of tsunami earthquakes. Prada et al. (2021) modelled rupture dynamics considering the velocity model of Sallarès and Ranero (2019) and supported their hypothesis, however, Meng and Duan (2023) pointed out that no significant effect of shallow modulus reduction on rupture velocity and deficiency in high-frequency radiation was found because extreme modulus reduction is only in the upper ~3 km below the seafloor. In fact, both Prada et al. (2021) and Meng and Duan (2023) showed significant strength drop, large slip rate and near-field ground motion when a compliant hanging wall due to low modulus is present (Ma and Beroza, 2008). Instead, Meng and Duan (2023) showed that conditionally stable region can be more effective in leading to slow rupture propagation and deficiency in high-frequency radiation in tsunami earthquakes, but this model may not be able to explain large tsunamigenesis without large shallow slip because the model is purely elastic.

In another recent study, Cheung et al. (2021) used the same qualitative concept of low-rigidity sediment in causing large shallow slip while maintaining seismic moment fixed to explain large tsunamigenesis. They claimed that the low rigidity of sediments is able to lead to extremely large slip to explain nearly all tsunami size variations observed in recent interplate thrust earthquakes. In doing so, they also reduced the fault area to increase slip (e.g., Satake and Tanioka, 1999) while keeping the moment constant. Little attention was paid to the physics involved in leading to the extremely large shallow slip, perhaps motivated by the large slip observations in the 2011 Tohoku-Oki earthquake while overlooking the key differential bathymetry observations in the northern Japan Trench. They concluded that rapid estimation of shallow slip with available geophysical data is important if reliable warning of local tsunami is to be realized. Clearly, this can mislead tsunami hazard assessments and mitigation efforts if the physics of tsunamigenesis is misunderstood.

Dynamic weakening mechanisms, such as thermal pressurization, have also been proposed in explaining large shallow slip (e.g., Noda and Lapusta, 2013). The model of Noda and Lapusta (2013) was in a full space, which ignored the importance of the free surface and is probably not likely to capture the essential rupture dynamics at shallow depths. Kubota et al. (2022) showed that dynamic weakening mechanisms lead to large stress drop at shallow depths inconsistent with the tsunami data recorded at the 7 OBP stations. The free surface and a compliant hanging wall due to wedge sediments can naturally lead to large shallow slip on a shallowly dipping fault without large stress drop (Ma and Beroza, 2008), as shown here for near-trench region off Miyagi Prefecture, which was used by Ide et al. (2011) in explaining the large shallow slip of the 2011 Tohoku-Oki earthquake in their model.

Satake et al. (2013) inferred a 3-min delay of shallow slip required by the tsunami data in their inversion. Here the tsunami data (timing, width, and amplitude) can be well explained by a slow rupture velocity of ~850 m/s in the northern Japan Trench. This is reminiscent of the 2004 Sumatra earthquake and tsunami. Seno and Hirata (2007) proposed that inelastic deformation of sediments produces a slow rupture (~700 m/s) at shallow depth, giving rise to a total rupture duration ~2000 s, which can explain the deformation in the Andaman and Nicobar Islands observed ~30 min after the earthquake origin time. The shallow slow rupture is similar to a tsunami earthquake, producing large tsunami while radiating less high-frequency energy. In contrast, Lay et al. (2005) proposed that there is a ~ 30-min delay for the slip in the Andaman and Nicobar Islands. There were not near-field high-resolution tsunami data or differential bathymetry data to test both hypotheses, unlike in the 2011 Tohoku-Oki event, but the model presented here is more consistent with the hypothesis of Seno and Hirata (2007). The slow rupture velocity (shown also by Stein and Okal, 2005) seems not produced by a recent dynamic rupture model of the 2004 Sumatra earthquake (Ulrich et al., 2022), which may not fully capture the physics of tsunami generation in this earthquake. Okal (2013) inferred no slow nature of the 2011 Tohoku-Oki earthquake, which can be explained by the dominant potency release with a regular rupture velocity in the central rupture zone and small potency release of slow rupture in the northern Japan Trench (Fig. 15). Large tsunami off the Sanriku coast north of 39°N, however, is due to a slow rupture modelled here.

5. Conclusions

A minimalist dynamic rupture model for the 2011 M_W 9.1 Tohoku-Oki earthquake has been presented to explain the key observations of crustal deformation and tsunami caused by this earthquake. The model incorporates realistic fault geometry, bathymetry, velocity structure from the JIVSM and along-arc variation of sediment thickness in the Japan Trench. By adding a southwestward extension of velocity-weakening zone and four SMGAs to the heterogeneous stress drop model of Kubota et al. (2022) the dynamic rupture model with a standard rate-and-state friction is shown to explain the GPS, tsunami data, and the differential bathymetry observations well with minimum tuning. This simple model captures some essential features of the earthquake, which can be further improved when strong ground motion and high-rate GPS data are considered in the future.

The large shallow slip (>50 m) occurs updip from the hypocenter extending along trench for ~200 km (between ~37°N and ~ 38.7°N), driven by a large patch of stress drop (up to ~10 MPa) near the hypocenter. The stress drop in the shallow part of large slip zone is significantly smaller (<~3 MPa). The large shallow slip is mainly caused by the large fault width, free surface, and compliant wedge sediments. The peak near-trench slip reaches 75.67 m, located ~50 km north of the trench directly updip from the hypocenter, consistent with the differential bathymetry observations. This ~50 km offset can be explained by the northwardly increasing sediment thickness in the Japan Trench and nearly elastic wedge response in the central rupture zone.

The along-arc variation of sediment thickness in the Japan Trench exerts a fundamental control on the variation of near-trench slip and tsunamigenesis along strike. The model reveals the important role of inelastic deformation of thick wedge sediment in causing slow rupture

propagation and efficient tsunamigenesis with diminishing slip north of ~38.5°N. The rupture velocity slows down to ~850 m/s in the thick sediment, which is significantly less than the shear wave speed of the sediment (1500 m/s). The slow rupture is largely due to plastic dissipation of energy within the wedge, which can be viewed as a slowly moving bulldozer pushing soil or snow in front of it to reach a critical state while dissipating energy. Similar to previous inelastic wedge deformation results, inelastic deformation generates large short-wavelength uplift (~4 m) efficiently with diminishing shallow slip at the trench, consistent with the differential bathymetry observations in the northern Japan Trench. This large inelastic uplift generates impulsive tsunami consistent with the signals recorded at 2 OBP stations (TM1 and TM2) and 3 GPS buoys (807, 804, and 802) off the Sanriku coast in terms of amplitude, width, and timing. Previous kinematic slip models also fit the data based on elastic dislocation theory, but used ~36 m slip at the trench, inconsistent with the differential bathymetry observations. The extreme runup north of 39°N can be due to amplification of short-wavelength (impulsive) tsunami by the rugged Sanriku coast. Therefore, inelastic wedge deformation of thick sediment in the northern Japan Trench provides a self-consistent mechanism for the generation of mysterious large tsunami along the Sanriku coast without large shallow slip at the trench.

The physics of tsunami earthquakes and large tsunamigenesis may be misunderstood in previous kinematic slip models for the 2011 Tohoku-Oki earthquake and some recent studies for global tsunamigenic earthquakes. There is a tendency in using elastic dislocation models and large shallow slip at trench in modeling nearly all large tsunamigenic earthquakes with little attention to the applicability and plausibility of elastic dislocation theory. This should be cautioned as it can severely mislead tsunami hazard assessments and mitigation efforts, e.g., in designing tsunami early warning systems. Inelastic wedge deformation, a mechanism that can explain the key observations in the 2011 Tohoku-Oki earthquake and anomalous earthquake characteristics associated with large tsunami generation, may need to be considered in dealing with tsunami hazards in sediment-rich margins around the world (e.g., Scholl et al., 2015; Qiu and Barbot, 2022).

Supplementary data to this article can be found online at https://doi.org/10.1016/j.tecto.2023.230146.

CRediT authorship contribution statement

Shuo Ma: Writing – review & editing, Writing – original draft, Visualization, Validation, Supervision, Software, Resources, Project administration, Methodology, Investigation, Funding acquisition, Formal analysis, Data curation, Conceptualization.

Declaration of Competing Interest

The authors declare that they have no known competing financial interests or personal relationships that could have appeared to influence the work reported in this paper.

Data availability

This work uses the same data sets as in Kubota et al. (2022); the detailed source information of the data was given in that paper. The source codes and input files to produce the models in this paper and model results (final fault slip, stress changes on fault, surface displacements, and moment density tensors associated with inelastic strain in the wedge) are available at https://doi.org/10.5281/zenodo.10201759.

Acknowledgements

With profound sadness, lasting respect, and precious memory, the author dedicates this paper to the late Dr. Dudley Joe Andrews for being a mentor, an inspirer, and a kindred spirit. He was one of the very few people who recognized the importance of the author's 2D inelastic deformation work on tsunamigenesis in 2012. The late Dr. Tetsuzo Seno suggested the variation of sediment thickness in the Japan Trench in 2016, which made this work possible. The author is grateful to Tatsuya Kubota and Tatsuhiko Saito for stimulating discussions, answering questions about their model, and hosting his recent sabbatical visit at NIED. Steve Day, Eric Dunham, and an anonymous reviewer provided helpful comments that greatly improved the paper. Yue Du fitted the backstop surface and helped with data preparation. Shiying Nie assisted with the derivation of the analytical solution in the Appendix. Hiroe Miyake, Kimiyuki Asano, and Aitaro Kato kindly provided their model results. This work was supported by the National Science Foundation (award no. EAR-2244703).

Appendix A. An analytical solution for a noncohesive critical wedge in 3D subject to the Drucker-Prager yield criterion

Dahlen (1984) presented an analytical solution for a noncohesive critical Coulomb wedge in 2D. Here I extend that solution to a 3D noncohesive critical wedge subject to the Drucker-Prager yield criterion (Eq. 8), where the maximum compressive stress is not perpendicular to wedge strike. For a 3D wedge with a constant surface slope (α) and fault dip (β) (Fig. A1) the governing equilibrium equation is given by

$$\begin{aligned}\frac{\partial\sigma_{xx}}{\partial x}+\frac{\partial\sigma_{xy}}{\partial y}+\frac{\partial\sigma_{xz}}{\partial z}&=-\rho g\sin\alpha,\\ \frac{\partial\sigma_{xy}}{\partial x}+\frac{\partial\sigma_{yy}}{\partial y}+\frac{\partial\sigma_{yz}}{\partial z}&=0,\\ \frac{\partial\sigma_{xz}}{\partial x}+\frac{\partial\sigma_{yz}}{\partial y}+\frac{\partial\sigma_{zz}}{\partial z}&=\rho g\cos\alpha,\end{aligned}\tag{A1}$$

where ρ is density and g is gravitational acceleration. The coordinate system is shown in Fig. A1. Because all the stresses are independent of y the derivatives with respect to y in (A1) vanish. The first and the third equations in (A1) reduce to the same equations as in Dahlen (1984). Therefore, the two stress solutions in Dahlen (1984) are valid in 3D:

$$\sigma^{*}_{zz}=(1-\lambda)\rho gz\cos\alpha\tag{A2}$$

$$\sigma_{xz}=-(\rho-\rho_{w})gz\sin\alpha,\tag{A3}$$

where the pore pressure ratio $\lambda=\frac{p-\rho_w gD}{-\sigma_{zz}-\rho_w gD}$, p is pore pressure, D is ocean depth to the surface slope (positive downward), and ρ_w is water density. All the shear and effective stresses are not a function of x, therefore the second equation of (A1) gives rise to

$$\sigma_{yz} = 0. \tag{A4}$$

Note that D is a function of x and $\frac{\partial D}{\partial x} = \sin\alpha$, therefore $\frac{\partial \sigma_{xx}}{\partial x} = -\rho_w g \sin\alpha$ and the first equation in (A1) is satisfied.

The other stresses in 3D can be determined from the direction of the maximum compressive stress, $\vec{n} = \{n_x, n_y, n_z\}$, and the Drucker-Prager yield criterion. If $\vec{n}$ is a principal direction, we have

$$\begin{bmatrix} \sigma^*_{xx} & \sigma_{xy} & \sigma_{xz} \\ \sigma_{xy} & \sigma^*_{yy} & 0 \\ \sigma_{xz} & 0 & \sigma^*_{zz} \end{bmatrix} \begin{Bmatrix} 1 \\ k \\ m \end{Bmatrix} = \sigma \begin{Bmatrix} 1 \\ k \\ m \end{Bmatrix}, \tag{A5}$$

where $k = \frac{n_y}{n_x}$, $m = \frac{n_z}{n_x}$, and σ is the principal effective stress. From (A5) it can be shown that

$$\sigma = \frac{1}{m}\sigma_{xz} + \sigma^*_{zz} \tag{A6}$$

$$\sigma^*_{xx} = \sigma^*_{zz} - k\sigma_{xy} + \left(\frac{1}{m} - m\right)\sigma_{xz} \tag{A7}$$

$$\sigma^*_{yy} = \sigma^*_{zz} - \frac{1}{k}\sigma_{xy} + \frac{1}{m}\sigma_{xz}. \tag{A8}$$

By substituting (A7) and (A8) into the Drucker-Prager yield criterion σ_{xy} can be solved. There are two solutions of σ_{xy}, choose the one solution that corresponds to the maximum compressive stress. Then from (A7) and (A8) all the stresses are obtained, and the 3D solution is complete.

The shear and normal stresses at the base of the wedge can be obtained by rotating the stress:

$$\sigma^*_{z'z'} = \frac{\sigma^*_{xx} + \sigma^*_{zz}}{2} - \frac{\sigma^*_{xx} - \sigma^*_{zz}}{2}\cos[2(\alpha+\beta)] - \sigma_{xz}\sin[2(\alpha+\beta)] \tag{A9}$$

$$\sigma_{z'x'} = -\frac{\sigma^*_{xx} - \sigma^*_{zz}}{2}\sin[2(\alpha+\beta)] + \sigma_{xz}\cos[2(\alpha+\beta)] \tag{A10}$$

$$\sigma_{z'y'} = -\sigma_{xy}\sin(\alpha+\beta), \tag{A11}$$

from which the ratio of shear to normal stresses at the base can be obtained by

$$\mu_b = -\frac{\sqrt{\sigma^2_{x'z'} + \sigma^2_{y'z'}}}{\sigma^*_{z'z'}}, \tag{A12}$$

which is the fault friction if the same pore pressure ratio λ is on the fault.

Alternatively, if the ratio of two shear stresses on the fault is known (equivalent to knowing the direction of shear stress on the fault), i.e.,

$$r = \frac{\sigma_{z'y'}}{\sigma_{z'x'}}, \tag{A13}$$

σ_{xy} can be directly determined when (A7) is used in (A10). Again, the other two stresses can be determined from (A7) and (A8). If μ_b is specified, the pore pressure ratio λ can be calculated from (A12). When we substitute all the stresses into the Drucker-Prager yield criterion the internal friction can be obtained, and the 3D solution is complete.

In order to apply the 3D wedge solution to the Japan Trench, surface slope and fault dip of the wedge need to be known. It can be seen from Fig. 2 that the northern Japan Trench is remarkably straight, with a strike ~5°, which makes this analytical solution easily applicable. All the nodes on the seafloor and fault (excluding the artificial 10° dipping surface near the trench) within 65 km from the trench at 50 km $\leq y \leq$ 250 km in the finite-element mesh are projected onto a plane perpendicular to the trench (Fig. A2). Then the points of surface slope and fault are fitted by two straight lines, which gives rise to α=4.6967° and β=4.4957°.

In the model for the northern Japan Trench, I specify $r = \tan(-5°)$, i.e., shear stress vector is along 5° clockwise from the trench-perpendicular direction on the fault, causing a small left-lateral strike-slip component (Fig. A1). The direction of maximum compressive stress is along plate convergence, which has an azimuth 105° (measured from $+y$ in Fig. A1) and makes an angle of inclination 15° from surface slope (corresponding to an inclination angle of 23.86° from the fault). The wedge density is the same as that of sediment in the outer wedge, $\rho = 2250$ kg/m^3. I specify $\mu_b = f_0 = 0.25$, which directly give rise to $\lambda = 0.7541$ (modest fluid overpressure) and $tan\phi = 0.3291$. Fig. A1 shows the actual geometry of the wedge with the determined α and β and three principal effective stresses calculated from the above in the same spatial scales. The minimum compressive stress is more vertical than the other two principal stress, with an angle of inclination of 62.18° from the horizontal plane. The principal effective stress ratios are $\frac{\sigma_3}{\sigma_1} = 0.5602$ and $\frac{\sigma_2}{\sigma_1} = 0.6573$, respectively.

Dahlen (1984) introduced another parameter, λ_b, which is the pore pressure ratio on the fault. He envisioned that there can be an abrupt pore pressure change across the fault, i.e., $\lambda_b \neq \lambda$. Therefore, the effective normal stress $\sigma^*_{z'z'}$ calculated from the bottom of the wedge in (A9) can be different from the effective normal stress on the fault. In this work, the effective normal stress on the fault ($\sigma_N^{0,*}$) uses the result shown in Fig. 5b, which can be thought of as due to a heterogeneous distribution of λ_b on the fault. Similarly, the shear stress on the fault in the model is calculated from μ_b and $\sigma_N^{0,*}$, different from the shear stress at the bottom of the wedge given by eqs. (A10 and 11), which can be caused by the various fault zone complexities (such

as horst and graben structure and stress, material, and rheology heterogenies) not captured by the simple critical wedge solution here. The 3D analytical solution presented above is only applied to the wedge in this work.

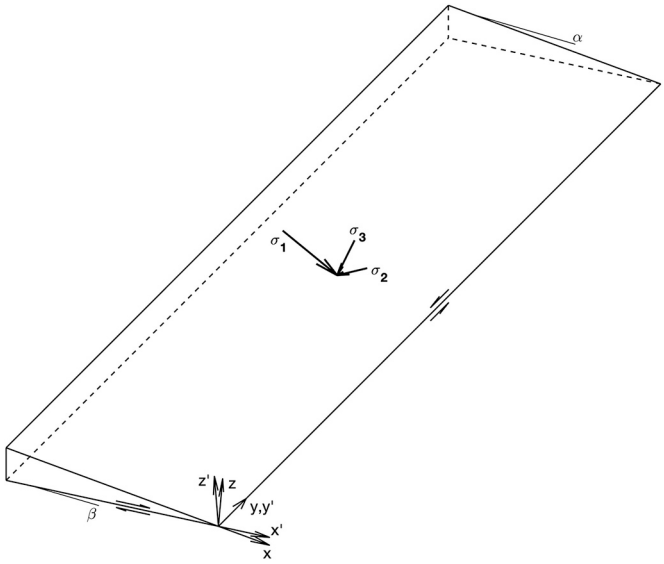

Fig. A1. A schematic geometry of a 3D critical wedge with constant surface slope α and fault dip β. The two coordinate systems shown are such that the x axis is along surface slope and x' along fault. The 3 principal effective stresses acting in the wedge are shown.

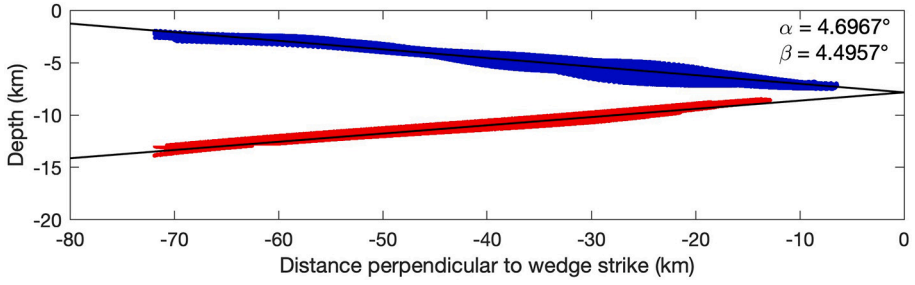

Fig. A2. The fitting of surface slope and fault dip of the wedge (inner and outer wedges treated as a whole) in the northern Japan Trench is shown. The blue and red dots show the nodes in the finite-element mesh on the surface slope and fault, respectively, projected onto a plane normal to wedge strike. (For interpretation of the references to colour in this figure legend, the reader is referred to the web version of this article.)

References

Andrews, D.J., 2005. Rupture dynamics with energy loss outside the slip zone. J. Geophys. Res. Solid Earth 110 (1). https://doi.org/10.1029/2004JB003191.

Bilek, S.L., Lay, T., 1998. Variation of interplate fault zone properties with depth in the Japan Subduction Zone. Science 281 (5380), 1175–1178. https://doi.org/10.1126/science.281.5380.1175.

Bilek, S.L., Lay, T., 1999. Rigidity variations with depth along interplate megathrust faults in subduction zones. Nature 400, 443–446.

Cheung, K.F., Lay, T., Sun, L., Yamazaki, Y., 2021. Tsunami size variability with rupture depth. Nat. Geosci. 15 (1), 33–36. https://doi.org/10.1038/s41561-021-00869-z.

Dahlen, F.A., 1984. Noncohesive critical Coulomb wedges: an exact solution. J. Geophys. Res. 89 (B12), 10125–10133. https://doi.org/10.1029/JB089iB12p10125.

Dahlen, F.A., 1990. Critical taper model of fold-and-thrust belts and accretionary wedges. Annu. Rev. Earth Planet. Sci. 18 https://doi.org/10.1146/annurev.ea.18.050190.000415.

DeMets, C., Gordon, R.G., Argus, D.F., 2010. Geologically current plate motions. Geophys. J. Int. 181, 1–80. https://doi.org/10.1111/j.1365-246X.2009.04491.x.

Du, Y., Ma, S., Kubota, T., Saito, T., 2021. Impulsive tsunami and large runup along the Sanriku coast of Japan produced by an inelastic wedge deformation model. J. Geophys. Res. Solid Earth 126 (8). https://doi.org/10.1029/2021jb022098.

Duan, B., 2012. Dynamic rupture of the 2011 Mw 9.0 Tohoku-Oki earthquake: Roles of a possible subducting seamount. J. Geophys. Res. Solid Earth 117 (5). https://doi.org/10.1029/2011JB009124.

Drucker, D.C., Prager, W., 1952. Soil mechanics and plastic analysis or limit design. Q. Appl. Math. 10, 157–165.

Dunham, E.M., Favreau, P., Carlson, J.M., 2003. A supershear transition mechanism for cracks. Science 299 (5612), 1557–1559. https://doi.org/10.1126/science.1080650.

Dunham, E.M., Belanger, D., Cong, L., Kozdon, J.E., 2011. Earthquake ruptures with strongly rate-weakening friction and off-fault plasticity, part 2: Nonplanar faults. Bull. Seismol. Soc. Am. 101 (5), 2308–2322. https://doi.org/10.1785/0120100076.

Fujii, Y., Satake, K., Watada, S., Ho, T.-C., 2021. Re-examination of slip distribution of the 2004 Sumatra–Andaman earthquake (M_W 9.2) by the inversion of tsunami data using Green's functions corrected for compressible seawater over the Elastic Earth. Pure Appl. Geophys. 178 (12), 4777–4796. https://doi.org/10.1007/s00024-021-02909-6.

Fujiwara, T., 2021. Seafloor Geodesy from Repeated Multibeam Bathymetric Surveys: Application to Seafloor Displacement Caused by the 2011 Tohoku-Oki Earthquake. https://doi.org/10.3389/feart.2021.667666.

Fujiwara, T., Kodaira, S., No, T., Kaiho, Y., Takahashi, N., Kaneda, Y., 2011. The 2011 Tohoku-Oki earthquake: Displacement reaching the trench axis. Science. https://doi.org/10.1126/science.1211554.

Fujiwara, T., dos Santos Ferreira, C., Bachmann, A.K., Strasser, M., Wefer, G., Sun, T., Kodaira, S., 2017. Seafloor Displacement after the 2011 Tohoku-oki Earthquake in the Northern Japan Trench Examined by Repeated Bathymetric surveys. Geophys. Res. Lett. 44 (23) https://doi.org/10.1002/2017GL075839, 833–11.

Fukuyama, E., Hok, S., 2015. Dynamic overshoot near trench caused by large asperity break at depth. Pure Appl. Geophys. 172, 2157–2165. https://doi.org/10.1007/s00024-013-0745-z.

Galvez, P., Petukhin, A., Irikura, K., Somerville, P., 2019. Dynamic source model for the 2011 Tohoku earthquake in a wide period range combining slip reactivation with the short-period ground motion generation process. Pure Appl. Geophys. 177 (5), 2143–2161. https://doi.org/10.1007/s00024-019-02210-7.

Geist, E.L., Bilek, S.L., 2001. Effect of depth-dependent shear modulus on tsunami generation along subduction zones. Geophys. Res. Lett. 28, 1315–1318.

Harris, R.A., Day, S.M., 1997. Effects of a low-velocity zone on a dynamic rupture. Bull. Seismol. Soc. Am. 87 (5), 1267–1280. https://doi.org/10.1785/bssa0870051267.

Hirakawa, E., Ma, S., 2016. Dynamic fault weakening and strengthening by gouge compaction and dilatancy in a fluid-saturated fault zone. J. Geophys. Res. Solid Earth 121 (8), 5988–6008. https://doi.org/10.1002/2015jb012509.

Hirono, T., Tsuda, K., Tanikawa, W., Ampuero, J.P., Shibazaki, B., Kinoshita, M., et al., 2016. Near-trench slip potential of megaquakes evaluated from fault properties and conditions. Sci. Rep. 6, 28184.

Hooper, A., Pietrzak, J., Simons, W., Cui, H., Riva, R., Naeije, M., Terwisscha van Scheltinga, A., Schrama, E., Stelling, G., Socquet, A., 2013. Importance of horizontal seafloor motion on tsunami height for the 2011 Mw = 9.0 Tohoku-Oki earthquake. Earth Planet Sci. Lett. 361, 469–479. https://doi.org/10.1016/j.epsl.2012.11.013.

Ide, S., Baltay, A., Beroza, G.C., 2011. Shallow dynamic overshoot and energetic deep rupture in the 2011 M_W 9.0 Tohoku-Oki earthquake. Science 332. https://doi.org/10.1126/science.1207020.

Iinuma, T., Hino, R., Kido, M., Inazu, D., Osada, Y., Ito, Y., Ohzono, M., Tsushima, H., Suzuki, S., Fujimoto, H., Miura, S., 2012. Coseismic slip distribution of the 2011 off the Pacific coast of Tohoku earthquake (m9.0) refined by means of seafloor geodetic data. J. Geophys. Res. Solid Earth 117 (B7). https://doi.org/10.1029/2012jb009186.

Ikari, M.J., Kameda, J., Saffer, D.M., Kopf, A.J., 2015. Strength characteristics of Japan Trench borehole samples in the high-slip region of the 2011 Tohoku-oki earthquake. Earth Planet. Sci. Lett. 412, 35–41.

Ikehara, K., Usami, K., Kanamatsu, T., Arai, K., Yamaguchi, A., Fukuchi, R., 2018. Spatial variability in sediment lithology and sedi- mentary processes along the Japan Trench: use of deep-sea turbidite records to reconstruct past large earthquakes. Geol. Soc. Lond. Spec. Publ. 456 (1), 75–89. https://doi.org/10.1144/SP456.9.

Kajiura, K., 1963. Leading wave of a tsunami. Bull. Earthquake Res. Inst. 43, 535–571.

Kanamori, H., 1972. Mechanism of tsunami earthquakes. Phys. Earth Planet. Inter. 6 (5), 346–359. https://doi.org/10.1016/0031-9201(72)90058-1.

Kanamori, H., Kikuchi, M., 1993. The 1992 Nicaragua earthquake: a slow tsunami earthquake associated with subducted sediments. Nature 361, 714–716.

Kodaira, S., No, T., Nakamura, Y., Fujiwara, T., Kaiho, Y., Miura, S., Taira, A., 2012. Coseismic fault rupture at the trench axis during the 2011 Tohoku-oki earthquake. Nat. Geosci. 5 (9) https://doi.org/10.1038/ngeo1547.

Kodaira, S., Nakamura, Y., Yamamoto, Y., Obana, K., Fujie, G., No, T., Miura, S., 2017. Depth-varying structural characters in the rupture zone of the 2011 Tohoku-oki earthquake. Geosphere 13 (5). https://doi.org/10.1130/GES01489.1.

Kato, A., Igarashi, T., 2012. Regional extent of the large coseismic slip zone of the 2011 M_W 9.0 Tohoku-Oki earthquake delineated by on-fault aftershocks. Geophys. Res. Lett. 39 (15) https://doi.org/10.1029/2012gl052220.

Kodaira, S., Fujiwara, T., Fujie, G., Nakamura, Y., Kanamatsu, T., 2020. Large coseismic slip to the trench during the 2011 Tohoku-Oki Earthquake. Annu. Rev. Earth Planet. Sci. 48 (1), 321–343. https://doi.org/10.1146/annurev-earth-071719-055216.

Kodaira, S., Linuma, T., Imai, K., 2021. Investigating a tsunamigenic megathrust earthquake in the Japan Trench. Science 371, eabe1169. https://doi.org/10.1126/science.abe1169.

Koketsu, K., Miyake, H., Suzuki, H., 2012. Japan integrated velocity structure model version 1. In: Proceedings of the 15th world conference on earthquake engineering. https://www.iitk.ac.in/nicee/wcee/article/WCEE2012_1773.pdf.

Kozdon, J.E., Dunham, E.M., 2013. Rupture to the Trench: Dynamic rupture simulations of the 11 march 2011 Tohoku earthquake. Bull. Seismol. Soc. Am. 103 (2 B), 1275–1289. https://doi.org/10.1785/0120120136.

Kubota, T., Saito, T., Hino, R., 2022. A new mechanical perspective on a shallow megathrust near-trench slip from the high-resolution fault model of the 2011 Tohoku-Oki earthquake. Progr. Earth Planet. Sci. 9 (1) https://doi.org/10.1186/s40645-022-00524-0.

Kurahashi, S., Irikura, K., 2013. Short-period source model of the 2011 M_W 9.0 off the pacific coast of Tohoku earthquake. Bull. Seismol. Soc. Am. 103 (2B), 1373–1393. https://doi.org/10.1785/0120120157.

Lay, T., 2018. A review of the rupture characteristics of the 2011 Tohoku-oki Mw 9.1 earthquake. Tectonophysics. https://doi.org/10.1016/j.tecto.2017.09.022.

Lay, T., Kanamori, H., Ammon, C.J., Nettles, M., Ward, S.N., Aster, R.C., Sipkin, S., 2005. The great Sumatra-Andaman earthquake of 26 December 2004. Science. https://doi.org/10.1126/science.1112250.

Lay, T., Kanamori, H., Ammon, C.J., Koper, K.D., Hutko, A.R., Ye, L., Rushing, T.M., 2012. Depth-varying rupture properties of subduction zone megathrust faults. J. Geophys. Res. Solid Earth 117 (4). https://doi.org/10.1029/2011JB009133.

Lotto, G.C., Dunham, E.M., Jeppson, T.N., Tobin, H.J., 2017. The effect of compliant prisms on subduction zone earthquakes and tsunamis. Earth Planet. Sci. Lett. 458, 213–222. https://doi.org/10.1016/j.epsl.2016.10.050.

Ma, S., 2012. A self-consistent mechanism for slow dynamic deformation and large tsunami generation for earthquakes in the shallow subduction zone. Geophys. Res. Lett. 39 (11) https://doi.org/10.1029/2012GL051854.

Ma, S., 2022. Dynamic off-fault failure and tsunamigenesis at strike-slip restraining bends: Fully-coupled models of dynamic rupture, ocean acoustic waves, and tsunami in a shallow bay. Tectonophysics 838, 229496. https://doi.org/10.1016/j.tecto.2022.229496.

Ma, S., Andrews, D.J., 2010. Inelastic off-fault response and three-dimensional earthquake rupture dynamics on a strike-slip fault. J. Geophys. Res. 115, B04304. https://doi.org/10.1029/2009JB006382.

Ma, S., Beroza, G.C., 2008. Rupture dynamics on a bi-material interface for dipping faults. Bull. Seismol. Soc. Am. 98, 1642–1658. https://doi.org/10.1785/0120070201.

Ma, S., Hirakawa, E.T., 2013. Dynamic wedge failure reveals anomalous energy radiation of shallow subduction earthquakes. Earth Planet. Sci. Lett. 375, 113–122. https://doi.org/10.1016/j.epsl.2013.05.016.

Ma, S., Nie, S., 2019. Dynamic wedge failure and along-arc variations of tsunamigenesis in the Japan Trench margin. Geophys. Res. Lett. 46 (15), 8782–8790. https://doi.org/10.1029/2019GL083148.

MacInnes, B.T., Gusman, A.R., LeVeque, R.J., Tanioka, Y., 2013. Comparison of earthquake source models for the 2011 Tohoku event using tsunami simulations and near-field observations. Bull. Seismol. Soc. Am. 103 (2B), 1256–1274. https://doi.org/10.1785/0120120121.

Maeda, T., Furumura, T., Sakai, S., Shinohara, M., 2011. Significant tsunami observed at Ocean-bottom pressure gauges during the 2011 off the Pacific coast of Tohoku earthquake. Earth Planet. Spac. 63 (7), 803–808. https://doi.org/10.5047/eps.2011.06.005.

Meng, Q., Duan, B., 2023. Do upper-plate material properties or fault frictional properties play more important roles in tsunami earthquake characteristics? Tectonophysics 850, 229765. https://doi.org/10.1016/j.tecto.2023.229765.

Mori, N., Takahashi, T., Yasuda, T., Yanagisawa, H., 2011. Survey of 2011 Tohoku earthquake tsunami inundation and run-up. Geophys. Res. Lett. https://doi.org/10.1029/2011GL049210.

Murphy, S., Scala, A., Herrero, A., Lorito, S., Festa, G., Trasatti, E., Tonini, R., Romano, F., Molinari, I., Nielsen, S., 2016. Shallow slip amplification and enhanced tsunami hazard unravelled by dynamic simulations of mega-thrust earthquakes. Sci. Rep. 6 (1) https://doi.org/10.1038/srep35007.

Noda, H., Lapusta, N., 2013. Stable creeping fault segments can become destructive as a result of dynamic weakening. Nature 493 (7433). https://doi.org/10.1038/nature11703.

Oglesby, D.D., Archuleta, R.J., Nielsen, S.B., 1998. Earthquakes on dipping faults: the effects of broken symmetry. Science 280 (5366). https://doi.org/10.1126/science.280.5366.1055.

Okal, E.A., 1988. Seismic parameters controlling far-field tsunami amplitudes: a Review. Nat. Hazards 1 (1), 67–96. https://doi.org/10.1007/bf00168222.

Okal, E.A., 2013. From 3-Hz *P* waves to ${}_0S_2$: No evidence of a slow component to the source of the 2011 Tohoku earthquake. Pure Appl. Geophys. 170, 963–973.

Polet, J., Kanamori, H., 2000. Shallow subduction zone earthquakes and their tsunamigenic potential. Geophys. J. Int. 142 (3) https://doi.org/10.1046/j.1365-246X.2000.00205.x.

Prada, M., Galvez, P., Ampuero, J., Sallarès, V., Sánchez-Linares, C., Macías, J., Peter, D., 2021. The influence of depth-varying elastic properties of the upper plate on megathrust earthquake rupture dynamics and Tsunamigenesis. J. Geophys. Res. Solid Earth 126 (11). https://doi.org/10.1029/2021jb022328.

Prakash, V., 1998. Frictional response of sliding interfaces subjected to time varying normal pressures. J. Tribol. 120 (1) https://doi.org/10.1115/1.2834197.

Qiu, Q., Barbot, S., 2022. Tsunami excitation in the outer wedge of global subduction zones. Earth Sci. Rev. 230, 104054 https://doi.org/10.1016/j.earscirev.2022.104054.

Saffer, D.M., Tobin, H.J., 2011. Hydrogeology and mechanics of subduction zone forearcs: Fluid flow and pore pressure. Annu. Rev. Earth Planet. Sci. 39 https://doi.org/10.1146/annurev-earth-040610-133408.

Saito, T., Inazu, D., Miyoshi, T., Hino, R., 2014. Dispersion and nonlinear effects in the 2011 Tohoku-Oki earthquake tsunami. J. Geophys. Res. Oceans 119 (8), 5160–5180. https://doi.org/10.1002/2014jc009971.

Sallarès, V., Ranero, C.R., 2019. Upper-plate rigidity determines depth-varying rupture behaviour of megathrust earthquakes. Nature 576 (7785), 96–101. https://doi.org/10.1038/s41586-019-1784-0.

Satake, K., Tanioka, Y., 1999. Sources of tsunami and tsunamigenic earthquakes in subduction zones. Pure Appl. Geophys. 154, 467–483.

Satake, K., Fujii, Y., Harada, T., Namegaya, Y., 2013. Time and space distribution of coseismic slip of the 2011 Tohoku earthquake as inferred from tsunami waveform data. Bull. Seismol. Soc. Am. 103 (2 B) https://doi.org/10.1785/0120120122.

Sato, M., Ishikawa, T., Ujihara, N., Yoshida, S., Fujita, M., Mochizuki, M., Asada, A., 2011. Displacement above the hypocenter of the 2011 Tohoku-Oki earthquake. Science 332 (6036), 1395. https://doi.org/10.1126/science.1207401.

Sawai, M., Niemeijer, A.R., Plumper, O., Hirose, T., Spiers, C.J., 2016. Nucleation of frictional instability caused by fluid pressurization in subducted blueschist. Geophys. Res. Lett. 43 (6), 2543–2551.

Scholl, D.W., Kirby, S.H., von Huene, R., Ryan, H., Wells, R.E., Geist, E.L., 2015. Great (Mw 8.0) megathrust earthquakes and the subduction of excess sediment and bathymetrically smooth seafloor. Geosphere 11 (2). https://doi.org/10.1130/GES01079.1.

Seno, T., 2000. The 21 September, 1999 Chi-Chi Earthquake in Taiwan: Implications for tsunami earthquakes. Terr. Atmos. Ocean. Sci. 11 (3), 701–708. https://doi.org/10.3319/TAO.2000.11.3.701(CCE).

Seno, T., Hirata, K., 2007. Did the 2004 Sumatra-Andaman earthquake involve a component of tsunami earthquakes? Bull. Seismol. Soc. Am. 97 (1 A SUPPL) https://doi.org/10.1785/0120050615.

Stein, S., Okal, E.A., 2005. Size and speed of the Sumatra earthquake. Nature 434, 581–582.

Sun, T., Wang, K., Fujiwara, T., Kodaira, S., He, J., 2017. Large fault slip peaking at trench in the 2011 Tohoku-oki earthquake. Nat. Commun. 8 https://doi.org/10.1038/ncomms14044.

Tanioka, Y., Satake, K., 1996. Tsunami generation by horizontal displacement of ocean bottom. Geophys. Res. Lett. 23 (8) https://doi.org/10.1029/96GL00736.

Tanioka, Y., Seno, T., 2001a. Detailed analysis of tsunami waveforms generated by the 1946 Aleutian tsunami earthquake. Nat. Hazards Earth Syst. Sci. 1 (4) https://doi.org/10.5194/nhess-1-171-2001.

Tanioka, Y., Seno, T., 2001b. Sediment effect on tsunami generation of the 1896 Sanriku tsunami earthquake. Geophys. Res. Lett. 28 (17) https://doi.org/10.1029/2001GL013149.

Tappin, D.R., Grilli, S.T., Harris, J.C., Geller, R.J., Masterlark, T., Kirby, J.T., Mai, P.M., 2014. Did a submarine landslide contribute to the 2011 Tohoku tsunami? Mar. Geol. 357 https://doi.org/10.1016/j.margeo.2014.09.043.

Tsuda, K., Iwase, S., Uratani, H., Ogawa, S., Watanabe, T., Miyakoshi, J., Ampuero, J.P., 2017. Dynamic rupture simulations based on the characterized source model of the 2011 Tohoku earthquake. Pure Appl. Geophys. 174 (9), 3357–3368. https://doi.org/10.1007/s00024-016-1446-1.

Tsuru, T., Park, J.-O., Miura, S., Kodaira, S., Kido, Y., Hayashi, T., 2002. Along-arc structural variation of the plate boundary at the Japan Trench margin: Implication of interplate coupling. J. Geophys. Res. Solid Earth 107 (B12), 2357. https://doi.org/10.1029/2001jb001664.

Uchida, N., Bürgmann, R., 2021. A decade of lessons learned from the 2011 tohoku-oki earthquake. Rev. Geophys. 59 (2) https://doi.org/10.1029/2020rg000713.

Ulrich, T., Gabriel, A.-A., Madden, E.H., 2022. Stress, rigidity and sediment strength control megathrust earthquake and tsunami dynamics. Nat. Geosci. 15 (1), 67–73. https://doi.org/10.1038/s41561-021-00863-5.

Viesca, R.C., Templeton, E.L., Rice, J.R., 2008. Off-fault plasticity and earthquake rupture dynamics: 2. Effects of fluid saturation. J. Geophys. Res. Solid Earth 113 (9). https://doi.org/10.1029/2007JB005530.

Wang, H.F., 2000. Theory of Linear Poroelasticity with Applications to Geomechanics and Hydrogeology. Princeton Univ. Press.

Wang, K., Hu, Y., 2006. Accretionary prisms in subduction earthquake cycles: the theory of dynamic Coulomb wedge. J. Geophys. Res. Solid Earth 111 (6). https://doi.org/10.1029/2005JB004094.

Wilson, A., Ma, S., 2021. Wedge plasticity and fully coupled simulations of dynamic rupture and tsunami in the Cascadia subduction zone. J. Geophys. Res. Solid Earth 126 (7). https://doi.org/10.1029/2020jb021627.

Yamazaki, Y., Cheung, K.F., Lay, T., 2018. A self-consistent fault slip model for the 2011 Tohoku Earthquake and tsunami. J. Geophys. Res. Solid Earth 123 (2). https://doi.org/10.1002/2017JB014749.

Yin, J., Denolle, M., 2021. The Earth surface controls the depth-dependent seismic radiation of megathrust earthquakes. AGU Advances 2, e2021AV000413. https://doi.org/10.1029/2021AV000413.

Yue, H., Lay, T., 2013. Source rupture models for the M_W 9.0 2011 Tohoku earthquake from joint inversions of high-rate geodetic and seismic data. Bull. Seismol. Soc. Am. 103 (2B), 1242–1255. https://doi.org/10.1785/0120120119.

Zhang, K., Wang, Y., Luo, Y., Zhao, D., Wang, M., Yang, F., Wu, Z., 2023. Complex tsunamigenic near-trench seafloor deformation during the 2011 Tohoku–Oki Earthquake. Nat. Commun. 14 (1) https://doi.org/10.1038/s41467-023-38970-z.